

# PPAR $\gamma$ lipodystrophy mutants reveal inter-molecular interactions required for enhancer activation

---

Received: 13 March 2022

---

Accepted: 7 November 2022

---

Published online: 19 November 2022

---

 Check for updates

---

Maria Stahl Madsen <sup>1,14</sup>, Marjoleine F. Broekema <sup>2,10,14</sup>, Martin Rønn Madsen <sup>1,11</sup>, Arjen Koppen <sup>2</sup>, Anouska Borgman<sup>2</sup>, Cathrin Gräwe <sup>3</sup>, Elisabeth G. K. Thomsen <sup>4</sup>, Denise Westland<sup>2</sup>, Mariette E. G. Kranendonk<sup>2,12</sup>, Marian Groot Koerkamp <sup>2,12</sup>, Nicole Hamers<sup>2</sup>, Alexandre M. J. J. Bonvin <sup>5</sup>, José M. Ramos Pittol <sup>2,13</sup>, Kedar Nath Natarajan <sup>1</sup>, Sander Kersten <sup>6</sup>, Frank C. P. Holstege <sup>2,12</sup>, Houshang Monajemi <sup>7,8</sup>, Saskia W. C. van Mil <sup>2</sup>, Michiel Vermeulen <sup>3</sup>, Birthe B. Kragelund <sup>4</sup>, David Cassiman <sup>9</sup>, Susanne Mandrup <sup>1,15</sup>  & Eric Kalkhoven <sup>2,15</sup> 

Peroxisome proliferator-activated receptor  $\gamma$  (PPAR $\gamma$ ) is the master regulator of adipocyte differentiation, and mutations that interfere with its function cause lipodystrophy. PPAR $\gamma$  is a highly modular protein, and structural studies indicate that PPAR $\gamma$  domains engage in several intra- and inter-molecular interactions. How these interactions modulate PPAR $\gamma$ 's ability to activate target genes in a cellular context is currently poorly understood. Here we take advantage of two previously uncharacterized lipodystrophy mutations, R212Q and E379K, that are predicted to interfere with the interaction of the hinge of PPAR $\gamma$  with DNA and with the interaction of PPAR $\gamma$  ligand binding domain (LBD) with the DNA-binding domain (DBD) of the retinoid X receptor, respectively. Using biochemical and genome-wide approaches we show that these mutations impair PPAR $\gamma$  function on an overlapping subset of target enhancers. The hinge region-DNA interaction appears mostly important for binding and remodelling of target enhancers in inaccessible chromatin, whereas the PPAR $\gamma$ -LBD:RXR-DBD interface stabilizes the PPAR $\gamma$ :RXR:DNA ternary complex. Our data demonstrate how in-depth analyses of lipodystrophy mutants can unravel molecular mechanisms of PPAR $\gamma$  function.

The nuclear receptor peroxisome proliferator-activated receptor  $\gamma$  (PPAR $\gamma$ ), encoded by the *PPARG* gene, is the master regulator of adipocyte differentiation and function and an important regulator of whole-body lipid metabolism and insulin sensitivity<sup>1</sup>. Agonists include several unsaturated fatty acids and lipid metabolites as well as various synthetic compounds such as insulin-sensitizing thiazolidinediones. The importance of PPAR $\gamma$  in human adipocyte biology and physiology is underscored by the finding that many cases of familial lipodystrophy, a syndrome characterized by repartitioning of adipose tissue

causing severe insulin resistance, type 2 diabetes mellitus (T2DM) and dyslipidemia, are caused by heterozygous point mutations in this transcription factor<sup>2</sup> (FPLD3; OMIM 604367).

PPAR $\gamma$  regulates transcription of its target genes by binding as a heterodimer with members of the retinoid X receptor (RXR) subfamily to PPAR-response elements (PPREs), which are degenerate repeats of 5'-AGGTCA-3' spaced by one nucleotide<sup>3,4</sup>. Here RXR occupies the 3' half site, while PPAR $\gamma$  binds to the 5' half site and its 5' extension<sup>5</sup>. In adipocytes, the PPAR $\gamma$ :RXR heterodimer cooperates with the CCAAT/

---

A full list of affiliations appears at the end of the paper.  e-mail: [s.mandrup@bmb.sdu.dk](mailto:s.mandrup@bmb.sdu.dk); [e.kalkhoven@umcutrecht.nl](mailto:e.kalkhoven@umcutrecht.nl)

enhancer-binding protein  $\alpha$  (C/EBP $\alpha$ ) in the activation of many target genes<sup>4</sup>. PPAR $\gamma$  and C/EBP $\alpha$  bind to many of the same target enhancers, in some cases in a highly interdependent manner. For most of these interdependent binding sites, C/EBP $\alpha$  acts as the leading transcription factor facilitating PPAR $\gamma$  binding; however, PPAR $\gamma$  can also act as a leading factor facilitating C/EBP $\alpha$  binding<sup>6</sup>.

Similar to other nuclear receptors, PPAR $\gamma$  is a modular protein composed of two highly structured and evolutionary conserved domains, the DNA-binding domain (DBD) and the ligand-binding domain (LBD), as well as two mostly unstructured and less conserved domains, the N-terminal A/B-domain and the hinge region<sup>7</sup>. While in vitro experiments indicate that the different domains of PPAR $\gamma$  can execute their functions independently, several results point to intra- and intermolecular interactions being important for transactivation by the full-length protein<sup>7-9</sup>. Early cell-based studies indicate intramolecular communication between the ligand-dependent transactivation

function in the LBD and the ligand-independent transactivation function in the N-terminus and showed that phosphorylation of S112 in the N-terminal domain can affect ligand binding<sup>10</sup>. Furthermore, studies of the structure of the DNA-bound PPAR $\gamma$ :RXR heterodimer using either X-ray crystallography or small-angle X-ray scattering (SAXS) indicate that several different intermolecular interfaces (DNA-protein and protein-protein) are directly involved in regulating PPAR $\gamma$  activity<sup>11-14</sup>. Thus, the structures indicate that the hinge domain of PPAR $\gamma$  contributes to specificity in DNA-binding by making contacts to the bases in the minor groove of the 5' extension of the PPRE<sup>11-13</sup>. Furthermore, these studies also indicate that heterodimerization involves several domains of both PPAR $\gamma$  and RXR. X-ray crystallography<sup>11</sup> and SAXS<sup>14</sup> revealed a compact, "closed" conformation of the DNA-bound heterodimer with three dimerization interfaces involving (i) the RXR $\alpha$  LBD (helix 10) and the PPAR $\gamma$  LBD (helix 10 and 11); (ii) the RXR $\alpha$  DBD and the PPAR $\gamma$  DBD (bridged by the DNA); and (iii) the RXR $\alpha$  DBD and the

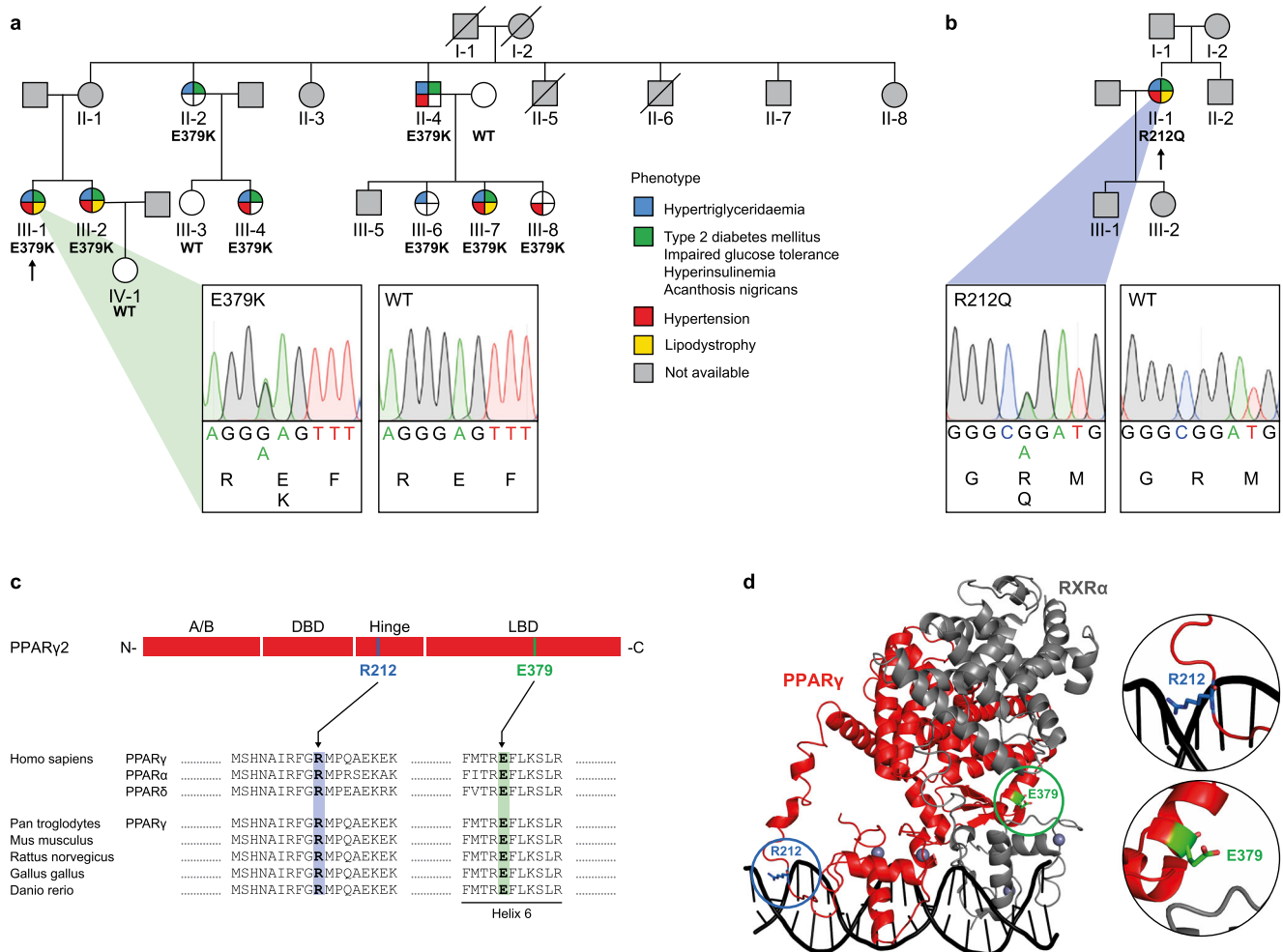


**Fig. 1 | Identification of PPAR $\gamma$ 2 E379K and R212Q.** **a** Family pedigree of index patient 1. Each family member is numbered for identification. The proband is indicated by an arrow. Squares and circles indicate males and females, respectively. Phenotypes are elaborated by color segments showing the presence of specific features. Gray symbols denote individuals that were not available for DNA analysis. Deceased individuals are indicated by a diagonal line through the symbol. DNA sequence analysis showing the heterozygous E379K mutation. The chromatogram shows both alleles from the patient (left panel) in comparison with corresponding genomic DNA from a non-affected individual (right panel). For tracing, the nucleotide and amino acid sequences are shown. **b** Family pedigree of index patient 2, harboring a heterozygous R212Q mutation. See description of panel a for details on representation. **c** Top: Schematic representation of domains in PPAR $\gamma$ 2; N-terminal A/B-domain, DNA-binding domain (DBD), hinge region, and ligand-

binding domain (LBD) and indicated positions of the two mutations. Bottom: Alignment of the amino acid sequence surrounding PPAR $\gamma$ 2 E379K and R212Q between human PPAR subtypes and PPAR $\gamma$  between different species. Residue positions of E379 and R212 are highlighted in green and blue, respectively. **d** Crystal structure of PPAR $\gamma$ :RXR $\alpha$  heterodimer bound to DNA (PPAR $\gamma$  in red; RXR $\alpha$  in gray; PDB entry 3DZY)<sup>11</sup>. E379 (in green) at the end of helix 6 in PPAR $\gamma$  at the heterodimerization interface with RXR $\alpha$  DBD and R212 (in blue) in the hinge region of PPAR $\gamma$  are encircled. Both amino acid residues are indicated in stick format. Protein Database entry 3DZY. The figure is generated by open-source software PyMOL2 ([www.pymol.org](http://www.pymol.org)). A similar DNA-bound conformation based on SAXS was proposed by Bernardes et al.<sup>14</sup>.

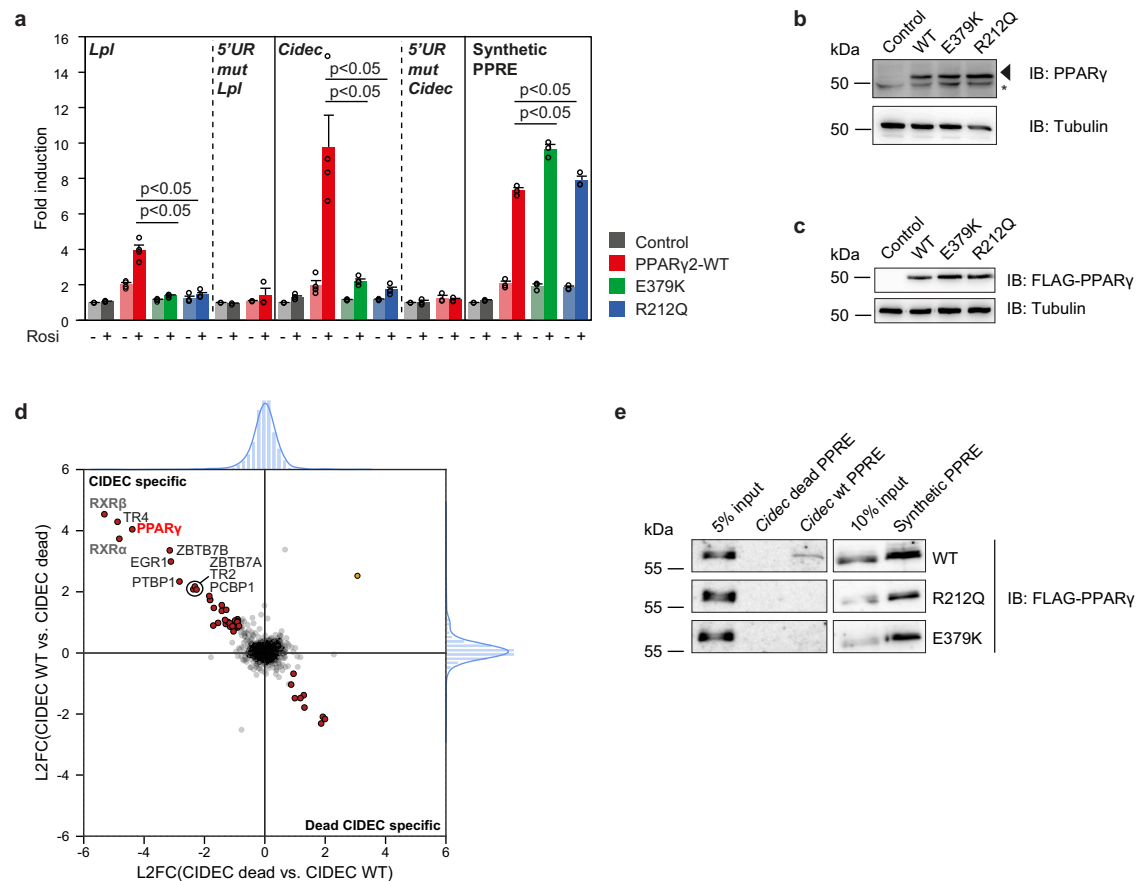


**Fig. 2 | E379K and R212Q mutants destabilize PPAR $\gamma$ :RXR binding to DNA in vitro.** **a** U2OS cells were transiently cotransfected with expression vectors encoding PPAR $\gamma$ -WT or mutants and different reporter constructs as indicated, in the absence or presence of 1  $\mu$ M rosiglitazone. Activation of the reporter is expressed as fold induction over that with empty vector (control). Data are presented as mean values + SEM, with individual data points indicated with circles,  $n = 3$ –4 biologically independent experiments. One-way ANOVA with Tukey’s multiple comparisons were used to compare cells transfected with mutant vs. WT; \* $p < 0.05$  cells transfected with mutant vs. WT. **b** Expression of the different PPAR $\gamma$  proteins transiently overexpressed in U2OS cells, as assessed by western blot. The arrow indicates PPAR $\gamma$ , and the asterisk indicates a non-specific band. Control, empty vector control; WT, PPAR $\gamma$  wild-type. Three independent experiments were performed and similar results were obtained. **c** Expression of the different FLAG-tagged PPAR $\gamma$  proteins stably overexpressed in U2OS cells, as assessed by western blot using a FLAG-tag antibody. Control, empty vector control; WT, wild-type.

Three independent experiments were performed and similar results were obtained. **d** DNA affinity purification-mass spectrometry analysis of *Cidec* PPARE interactors. Forward and reverse experiments were performed using oligonucleotides containing the *Cidec* PPARE motif or a mutant version (*Cidec* dead), followed by dimethyl labeling and mass spectrometry analysis. Log<sub>2</sub> ratios (L2FC) of all identified and quantified proteins (from nuclear extracts) in both experiments were plotted against each other. Proteins binding equally well to both oligonucleotides center around log<sub>2</sub>(ratio) = 0 and are marked in light gray. Proteins binding significantly better to the *Cidec* PPARE motif or the *Cidec* dead motif were determined by outlier statistics. These proteins are marked in red. **e** DNA affinity purification followed by western blot analysis were performed using oligonucleotides containing the *Cidec* PPARE motif, the *Cidec* dead motif and the synthetic PPARE motif. Pulldowns were performed using nuclear extracts containing the different FLAG-tagged PPAR $\gamma$  proteins. Three independent experiments were performed, and similar results were obtained. Source data for panel **a**–**c** and **e** are provided in the Source Data file.

PPAR $\gamma$  LBD (helix 6). This latter PPAR $\gamma$ :RXR LBD-DBD interaction, which was supported by hydrogen-deuterium (H/D) exchange mass spectrometry<sup>11,14</sup> and mutagenesis studies<sup>11</sup>, may critically depend on DNA binding, as it was not observed in the absence of DNA<sup>14</sup>. Furthermore, it should be noted that a more elongated, “open” conformation of the DNA-bound heterodimer lacking the PPAR $\gamma$ :RXR LBD-DBD interaction was reported in other SAXS studies, in this case supported by FRET studies<sup>12,13</sup>. More recently, LBD-DBD interdomain interactions were supported by analogy with the RAR $\beta$ :RXR heterodimer<sup>9</sup>. Regardless of these differences in structural approaches and data interpretation, it is currently poorly understood how complex intermolecular interactions may modulate the ability of PPAR $\gamma$  to activate target enhancers in cooperation with other transcription factors in the context of chromatin.

Here, we investigate the genome-wide epigenomic and transcriptional effects of two previously uncharacterized FPLD3-associated *PPARG* mutations, i.e., PPAR $\gamma$ -R212Q in the hinge region and PPAR $\gamma$ -E379K in the LBD, both predicted to interfere with

intermolecular interactions of the ternary PPAR $\gamma$ :RXR:DNA complex. We show that both mutations impair the adipogenic capacity of PPAR $\gamma$  as well as the activation of an overlapping subset of enhancers that are characterized by being highly dependent on PPAR $\gamma$  for chromatin remodeling. These findings provide mechanistic insights into the function of PPAR $\gamma$  and emphasize the importance of PPAR $\gamma$  as the leading transcription factor in a subset of target enhancers.

## Results

### Identification of the FPLD3-associated PPAR $\gamma$ mutations E379K and R212Q

FPLD3-associated *PPARG* mutations present a valuable tool to unravel the complex intermolecular interactions (both protein-protein and protein-DNA) required for optimal enhancer activation by PPAR $\gamma$  as they invariably result in loss of function<sup>2,15</sup>. We selected two previously uncharacterized FPLD3-associated *PPARG* mutations that are both predicted to affect intermolecular interactions based on structural studies. The first represents a novel heterozygous

missense FPLD3 mutation (Fig. 1a), substituting a highly conserved glutamic acid at position 379 in helix 6 in the LBD of PPAR $\gamma$  with a lysine (E379K; Fig. 1a, c). Genotyping showed the same mutation in seven additional family members, all of whom have derangements in lipid and glucose metabolism, whereas it was absent in family members without metabolic derangements (Fig. 1a). Crystallography and SAXS of the DNA-bound PPAR $\gamma$ :RXR $\alpha$  heterodimer have indicated that E379 is located at the heterodimerization interface between PPAR $\gamma$  LBD and RXR $\alpha$  DBD (Fig. 1d)<sup>11,14</sup>. An alternative conformation has been proposed in other SAXS studies, where E379 points outwards from the ternary complex (Supplementary Fig. 1)<sup>12</sup>.

The second heterozygous mutation we selected results in the substitution of a highly conserved arginine with glutamine (R212Q; Fig. 1b, c). Also, in this case, we identified this mutation in a patient with clear lipodystrophy features (Fig. 1b). Germline transmission could not be established as family members were unavailable for genotyping, but R212Q and R212W have previously been reported in FPLD3 patients by others<sup>15,16</sup>. Arginine 212 is located in the hinge region and forms interactions with the minor groove of the DNA helix immediately 5' of the PPRE (referred to as the 5' extension or 5' upstream region; 5' UR), and substitution of arginine with a glutamine residue may reduce these (Fig. 1d and Supplementary Fig. 1)<sup>11,12</sup>.

Taken together, we identified two previously uncharacterized lipodystrophy mutations that are predicted to interfere with two interaction interfaces of PPAR $\gamma$  that remain functionally poorly understood.

### E379K and R212Q mutants destabilize PPAR $\gamma$ :RXR binding to DNA in vitro

The fact that E379 and R212 residues are located in predicted, but functionally elusive interaction interfaces of PPAR $\gamma$ :RXR and PPAR $\gamma$ :DNA, respectively, prompted us to study the transcriptional and epigenomic effects of the E379K and R212Q lipodystrophy mutants in detail. We first investigated the effect of these two mutations on the ability of PPAR $\gamma$  to activate transcription in reporter assays in U2OS cells, which express negligible levels of endogenous PPAR $\gamma$ <sup>17</sup>. Cells were transiently transfected with expression plasmids encoding WT or mutant PPAR $\gamma$  and reporter constructs regulated by the well-established PPRE located in the promoter-proximal enhancers of the lipoprotein lipase (*Lpl*) gene<sup>3,18</sup> and the Cell Death Inducing DFFA Like Effector C gene (*Cidec*; also referred to as *Fsp27*)<sup>3,19</sup> (Supplementary Fig. 2). Both PPRES are imperfect repeats with partly conserved 5' extensions (Supplementary Fig. 2). Compared to WT PPAR $\gamma$ , the two mutants display greatly reduced ability to activate both reporter constructs (Fig. 2a) at comparable levels of expression (Fig. 2b). In agreement with previous data<sup>15</sup>, the FPLD3-associated R212W mutant also displays reduced activity (data not shown), similar to the R212Q mutant reported here. Consistent with the importance of the 5' extension for imperfect PPRES<sup>5,11,12</sup>, WT PPAR $\gamma$  loses its ability to activate the *Lpl* and *Cidec* PPRES when this sequence is mutated (Fig. 2a). Interestingly, however, both mutants readily activate a reporter containing a synthetic, perfectly palindromic PPRES identical to the one used for X-ray and SAXS structural studies<sup>5,11,12</sup>. These results indicate that the R212Q mutation, as well as E379K mutation, destabilizes the DNA-binding of PPAR $\gamma$  at imperfect PPRES.

To specifically compare the DNA-binding properties of the WT and mutant PPAR $\gamma$  proteins, we performed DNA pull-down assays. Nuclear extracts from U2OS cells stably expressing comparable levels of the different PPAR $\gamma$  proteins (Fig. 2c) were incubated and pulled down with the *Cidec* PPRES, a mutated *Cidec* PPRES, or the synthetic PPRES. Mass spectrometry analysis confirmed that the WT *Cidec* PPRES specifically pulled down PPAR $\gamma$  and RXR $\alpha$  and - $\beta$  (Fig. 2d), and western blotting showed that DNA binding of mutants is severely compromised on the *Cidec* PPRES but not on the synthetic PPRES (Fig. 2e). In support of the E379 residue being important in the DNA-bound state only<sup>14</sup>,

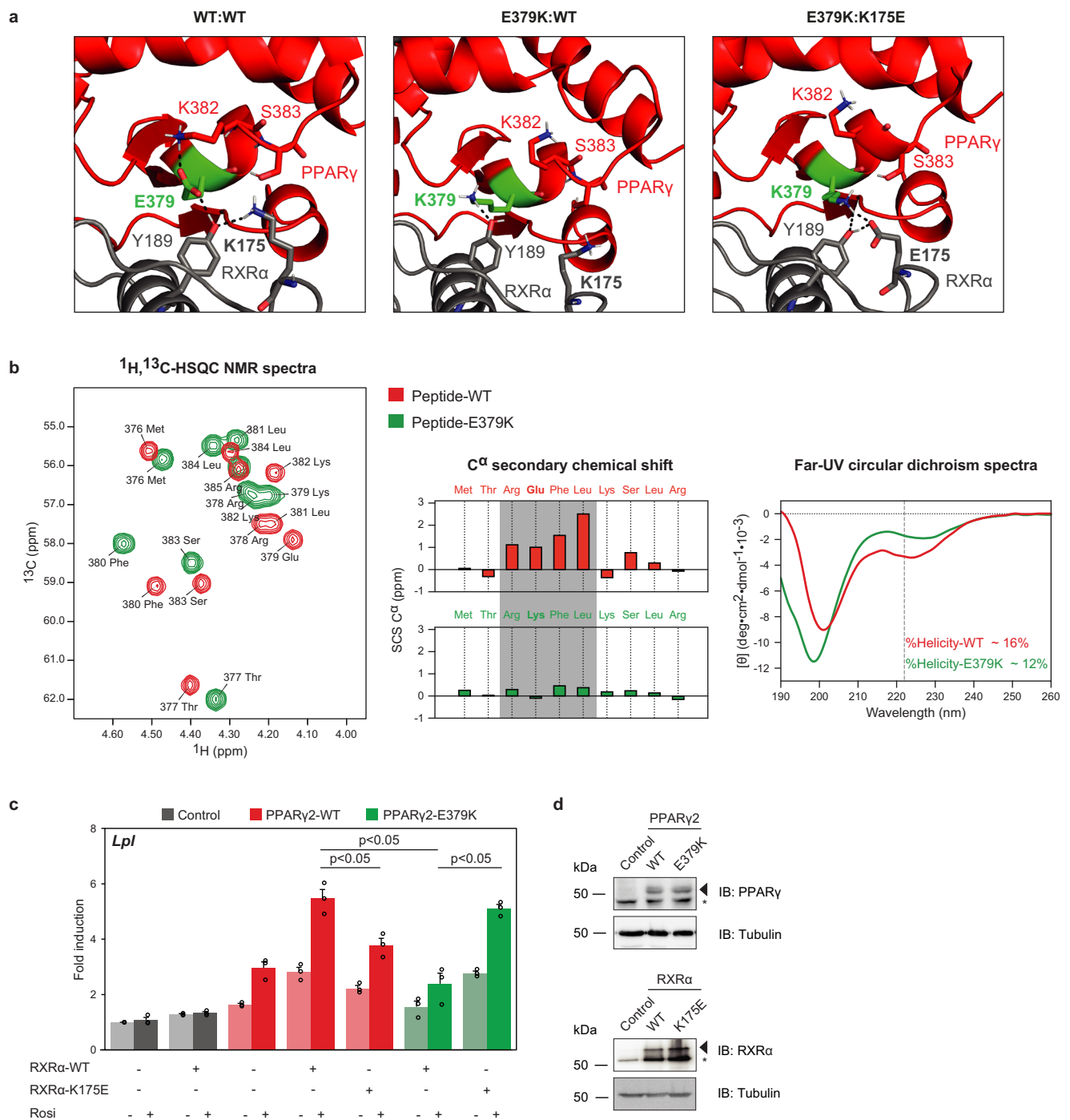
heterodimerization in the absence of DNA, which is known to critically depend on the PPAR $\gamma$ :RXR LBD-LBD interface<sup>17</sup>, was intact (Supplementary Fig. 3a–e). Furthermore, when tested in isolation, the PPAR $\gamma$ :RXR LBD-DBD interface was insufficient for efficient heterodimerization in vitro (Supplementary Fig. 3d). Taken together, these results indicate that although neither mutation affects the DBD, they both interfere with in vitro DNA binding on natural imperfect PPRES.

The finding that the R212Q mutant interferes with DNA binding is consistent with the predicted role of the N-terminal part of the hinge region in DNA binding to the 5' extension of the PPRES<sup>11,12</sup> (Fig. 1d and Supplementary Fig. 1). However, the E379 residue is located in the LBD and does not directly contact the DNA (Fig. 1d and Supplementary Fig. 1). Close inspection of the PPAR $\gamma$ :RXR $\alpha$  crystal structure shows a complex inter- and intramolecular interaction network involving a quartet of residues, where E379 interacts with a tyrosine in RXR $\alpha$  (Y189), with stabilizing intra-helical interactions between E379 and K382 in helix 6 of PPAR $\gamma$  and an intramolecular interaction between Y189 and K175 in RXR $\alpha$  (Fig. 3a). The importance of the stabilizing interaction within helix 6 was supported with spectroscopic NMR and CD data of WT and E379K peptides, with severe loss of helicity in the E379K peptide (Fig. 3b). Therefore, the E379K mutant is predicted to perturb this specific interaction interface with RXR $\alpha$  and is expected to lead to destabilization of the heterodimer:DNA complex. In silico predictions based on the crystal structure indicated a potential for compensation by an artificial charge reversal RXR $\alpha$ -K175E mutant, which would restore the important contact between RXR and helix 6 through a new electrostatic interaction between E379K<sub>PPAR $\gamma$</sub>  and K175E<sub>RXR $\alpha$</sub>  (Fig. 3a). Experimental testing of this model in HEK293T-cells, which express negligible levels of endogenous PPAR $\gamma$  and RXR $\alpha$ <sup>15</sup> revealed that the RXR $\alpha$ -K175E mutant displays a similar transcriptional defect as the PPAR $\gamma$ -E379K mutant (Fig. 3c, d). Interestingly, however, the combination of the two mutants rescued activation of the *Lpl* and the *Cidec* reporter (Fig. 3c, d and Supplementary Fig. 4), suggesting that the new PPAR $\gamma$ -K379/RXR $\alpha$ -E175 salt bridge can restore a functional PPAR $\gamma$ :RXR heterodimer. We wished to exclude additional functional defects of the E379K mutation and focused on ligand-dependent coregulator docking and subsequent transcriptional activation, two intertwined functions that are also mediated by the LBD and affected in several natural PPAR $\gamma$  mutants (e.g., refs. 20, 21). When testing the LBD in isolation, no clear functional defects of the E379K mutation were observed regarding ligand-dependent in vitro coregulator binding and transcriptional activity (Supplementary Fig. 5).

In summary, the PPAR $\gamma$  lipodystrophy-associated mutations R212Q and E379K, located in the hinge and LBD, respectively, both markedly destabilize the binding of the PPAR $\gamma$ :RXR heterodimer to natural imperfect PPRES but through effects on different interfaces.

### E379K and R212Q mutants impair adipogenic capacity of PPAR $\gamma$

To investigate how these mutations affect the epigenomic and transcriptional effects of PPAR $\gamma$  in chromatin, we took advantage of our recently developed model system based on immortalized PPAR $\gamma$ <sup>-/-</sup> mouse embryonic fibroblasts stably transduced to express high levels of coxackie adenoviral receptor (CAR) for efficient uptake of adenoviruses (PPAR $\gamma$ <sup>-/-</sup> MEF-CARs)<sup>6</sup>. We have previously shown that short-term exposure of these cells to adenoviruses expressing PPAR $\gamma$  leads to the activation of PPAR $\gamma$ -target enhancers and induction of many adipocyte genes. We, therefore, introduced the R212Q and E379K mutations into the corresponding sites in murine PPAR $\gamma$  and titrated the adenoviral vectors to express similar levels of WT and mutant PPAR $\gamma$  in PPAR $\gamma$ <sup>-/-</sup> MEF-CAR cells (Fig. 4a, b). Following 2 h of exposure to adenovirus, the medium was removed, and cells were stimulated with an adipogenic cocktail. Interestingly, after seven days of incubation, cells transduced with WT PPAR $\gamma$  accumulate lipids and express adipocyte marker genes, whereas differentiation is much less efficient in cells transduced with the mutant PPARs (Fig. 4c, d). These findings



indicate that the ability of PPAR $\gamma$  to drive adipocyte differentiation is impaired by both mutations but most markedly by the R212Q mutation.

### E379K and R212Q mutants compromise acute activation of a subset of target genes

To obtain molecular insights into the mechanisms underlying the reduced adipogenic potential of the PPAR $\gamma$  mutants (Fig. 4), we compared the ability of adenovirally expressed WT and mutant PPAR $\gamma$  to acutely activate gene expression in PPAR $\gamma^{-/-}$  MEF-CAR cells in the presence of rosiglitazone (Fig. 5a). In this setting, PPAR $\gamma$ -WT expression changes the expression of 399 genes (DESeq2, false discovery rate (FDR) < 5% and fold change PPAR $\gamma$ -WT vs Control  $\geq 1.5$  or  $\leq -1.5$ ), with 277 genes being induced and 122 genes being repressed compared to

control cells (Fig. 5b and Supplementary Tables 2, 3). For further analyses, we focused on the genes induced by PPAR $\gamma$ -WT, as the mechanisms underlying PPAR $\gamma$ -mediated gene repression are less well understood and likely indirect<sup>22,23</sup>. As expected, genes induced by PPAR $\gamma$ -WT are enriched in adipocyte-related GO-categories (e.g., lipid droplet organization, lipid storage, cellular triglyceride homeostasis, fat cell differentiation), and genes that contribute most to both PC1 and PC2 in the principal component analysis (PCA), are primarily genes related to adipocyte biology (Fig. 5c and Supplementary Table 4). Notably, and in line with the adipogenic effect (Fig. 4), cells expressing PPAR $\gamma$ -R212Q are closer to control cells in the PCA plot compared with cells expressing PPAR $\gamma$ -E379K (Fig. 5c), indicating that the R212Q mutant more dramatically affects the ability of PPAR $\gamma$  to acutely activate target genes (Fig. 5a).

**Fig. 3 | The PPAR $\gamma$ -E379K mutation alters interaction with RXR $\alpha$ .** **a** Structure analysis and computational modeling the crystal structure of an PPAR $\gamma$ :RXR $\alpha$  complex (PPAR $\gamma$  in red; RXR $\alpha$  in gray) bound to DNA using the HADDOCK2.2 web server shows a complex interaction network involving PPAR $\gamma$ -E379 and -K382 (LBD) and RXR $\alpha$ -Y189 and -K175 (DBD) in the WT complex (left panel). PPAR $\gamma$ -E379K alters the configuration of this interface (middle panel). Double charge reversal mutations in PPAR $\gamma$  (E379K) and RXR $\alpha$  (K175E) can restore the PPAR $\gamma$  LBD-RXR $\alpha$  DBD interface through a novel electrostatic interaction (right panel) (PDB entry 3DZY). Amino acid residues involved in the PPAR $\gamma$  LBD-RXR $\alpha$  DBD interface are indicated in the stick format. The figures were generated by PyMOL Molecular Graphics System Version 1.8 (2015) provided by SGrid<sup>60</sup>. **b** Spectroscopic analyses of helix 6 peptides. Left panel: <sup>1</sup>H, <sup>13</sup>C-HSQC spectra of PPAR $\gamma$ -WT<sup>376-385</sup> (red) and -PPAR $\gamma$ -E379K<sup>376-385</sup> (green) recorded in 20 mM Na<sub>2</sub>HPO<sub>4</sub> /NaH<sub>2</sub>PO<sub>4</sub> (pH 7.4) at 25 °C and overlaid. Signals originate from C $\alpha$ . Middle panel: The C $\alpha$  secondary chemical shifts (SCSs) for both the WT peptide (red) and the E379K variant (green)<sup>49</sup>. In the WT peptide, Arg378–Leu381 showed consecutive positive C $\alpha$  SCSs, indicating transient

helical structure (gray box). Right panel: Far-UV CD spectra of PPAR $\gamma$ -WT<sup>376-385</sup> (red) and PPAR $\gamma$ -E379K<sup>376-385</sup> (green) recorded at 25 °C in 20 mM Na<sub>2</sub>HPO<sub>4</sub>/NaH<sub>2</sub>PO<sub>4</sub> (pH 7.4). Dashed vertical line indicated the minimum at 222 nm for  $\alpha$ -helix structure. **c** HEK293T cells were transiently cotransfected with expression vectors encoding WT or mutant PPAR $\gamma$ , WT or mutant RXR $\alpha$ , and the *Lpl* PPRE-minimal promoter-reporter, in the absence or presence of 1  $\mu$ M rosiglitazone. Activation of the reporter is expressed as fold induction over empty vector (control). Data are presented as mean values + SEM, with individual data points indicated with circles,  $n = 3$  biologically independent experiments. One-way ANOVA with Tukey's multiple comparisons were used to compare cells transfected with mutant vs. WT; \* $p < 0.05$ . **d** Overexpression of the different PPAR $\gamma$  and RXR $\alpha$  proteins in HEK293T cells, as assessed by western blot analyses using a PPAR $\gamma$ - or RXR $\alpha$ - specific antibody. The arrows indicate PPAR $\gamma$  or RXR $\alpha$ , and the asterisk indicates an unknown non-specific band. Control, empty vector control; WT, wild-type. Three independent experiments were performed, and similar results were obtained. Source data for panel **b–d** are provided in the Source Data file.

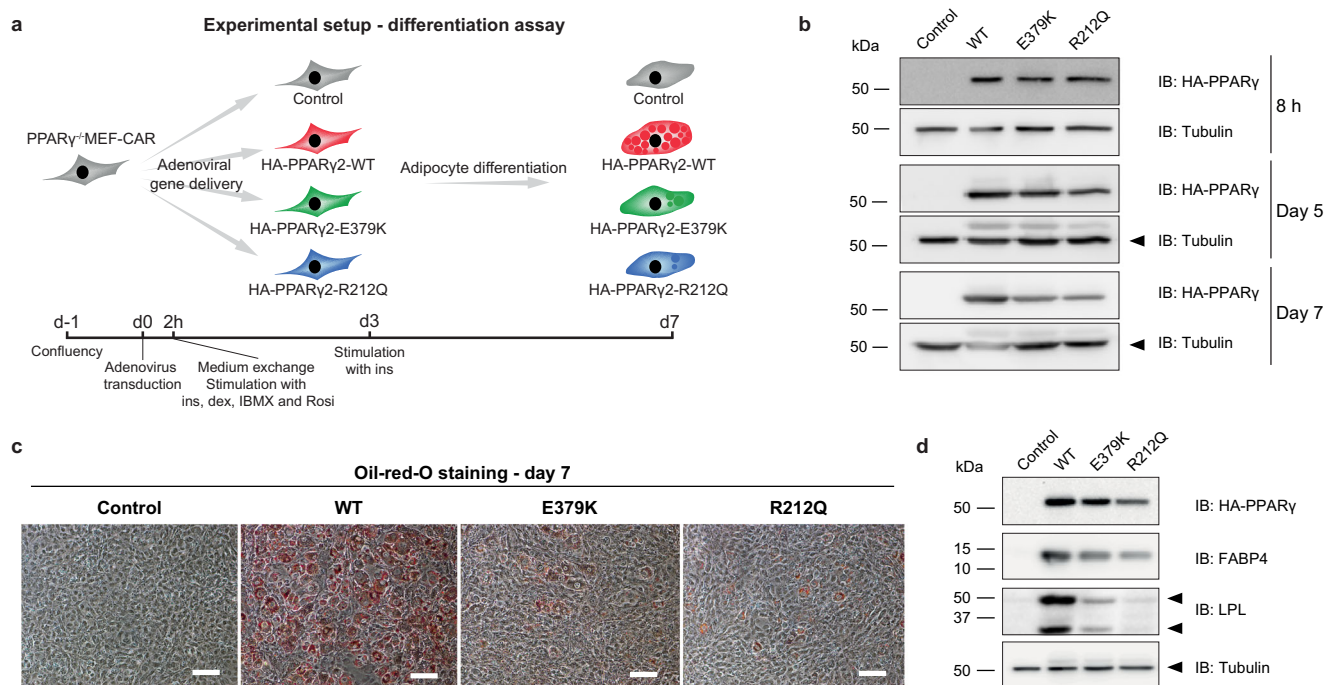


**Fig. 4 | E379K and R212Q impair the adipogenic capacity of PPAR $\gamma$ 2.**

**a** Experimental outline showing the timing of the transduction of PPAR $\gamma$ <sup>-/-</sup> MEF-CAR cells with adenovirus containing HA-tagged PPAR $\gamma$ 2-WT or mutants, and treatment of the transduced cells with the differentiation cocktails (2h-day 3: insulin, dexamethasone, isobutylmethylxanthine, and rosiglitazone, day 3–7: insulin). **b** Western blot assessing the expression of WT and mutant PPAR $\gamma$ 2 at the timepoints 8 h, day 5 and day 7 after adenoviral transduction. The membrane was probed with antibodies against HA-tagged PPAR $\gamma$  and Tubulin (internal control). Three independent experiments were performed, and similar results were

obtained. **c** Oil-red-O staining of lipid droplets at day 7 of differentiation. Three independent experiments were performed and similar results were obtained. Scale bar, 50  $\mu$ m. **d** Western blot 7 days after adenoviral transduction. The membrane was probed with antibodies against HA-tagged PPAR $\gamma$ , FABP4, LPL, and Tubulin (internal control). After correction for tubulin and PPAR $\gamma$  levels, relative protein levels for FABP4 were 77% (E379K) and 79% (R212Q) of WT levels, and for LPL 33% (E379K) and 28% (R212Q). Three independent experiments were performed and similar results were obtained. Source data for panel **b** and **d** are provided in the Source Data file.

The majority of the 277 PPAR $\gamma$ -WT induced genes, including the well-known PPAR target genes Krueppel-Like Factor 11 (*Klf11*)<sup>24</sup> and Uncoupling protein 2 (*Ucp2*)<sup>25</sup> were induced at comparable levels by the WT and mutant PPAR $\gamma$  proteins, and one gene (Pyruvate Dehydrogenase Kinase 4 (*Pdk4*)) was more induced by the mutants (Fig. 5d–f), demonstrating that mutant proteins retain some degree of functionality. Interestingly, however, 98 and 140 PPAR $\gamma$ -target genes are less induced by the E379K and R212Q mutant PPAR $\gamma$ , respectively (FDR < 5% and fold change mutant vs. WT < -1.25, Fig. 5d–f), with an overlap of 81 genes (Fig. 5g). This set of mutation-sensitive PPAR $\gamma$ -target genes includes several classic PPAR $\gamma$ -target genes like fatty acid binding protein 4 (*Fabp4*)<sup>26</sup>, *Lpl*<sup>18</sup>, *Cidec*<sup>19</sup>, and CCAAT/Enhancer-

binding protein alpha (*Cebpa*)<sup>27,28</sup> (Fig. 5c–f and Supplementary Table 5). Notably, most genes significantly affected by only the E379K mutation showed a tendency to be affected by the R212Q mutation, and vice versa (Fig. 5h). Together, the results indicate that the PPAR $\gamma$  mutations E379K and R212Q, which affect different domains of the PPAR $\gamma$  protein and different interaction interfaces, diminish the induction of a largely overlapping subset of PPAR $\gamma$ -target genes, while simultaneously retaining activation potential for other target genes. Notably, mutation-sensitive target genes are generally more induced upon PPAR $\gamma$ -WT expression compared to target genes that are changing less than 25% comparing activation by mutant and WT PPAR $\gamma$  (insensitive genes) (Fig. 5i).

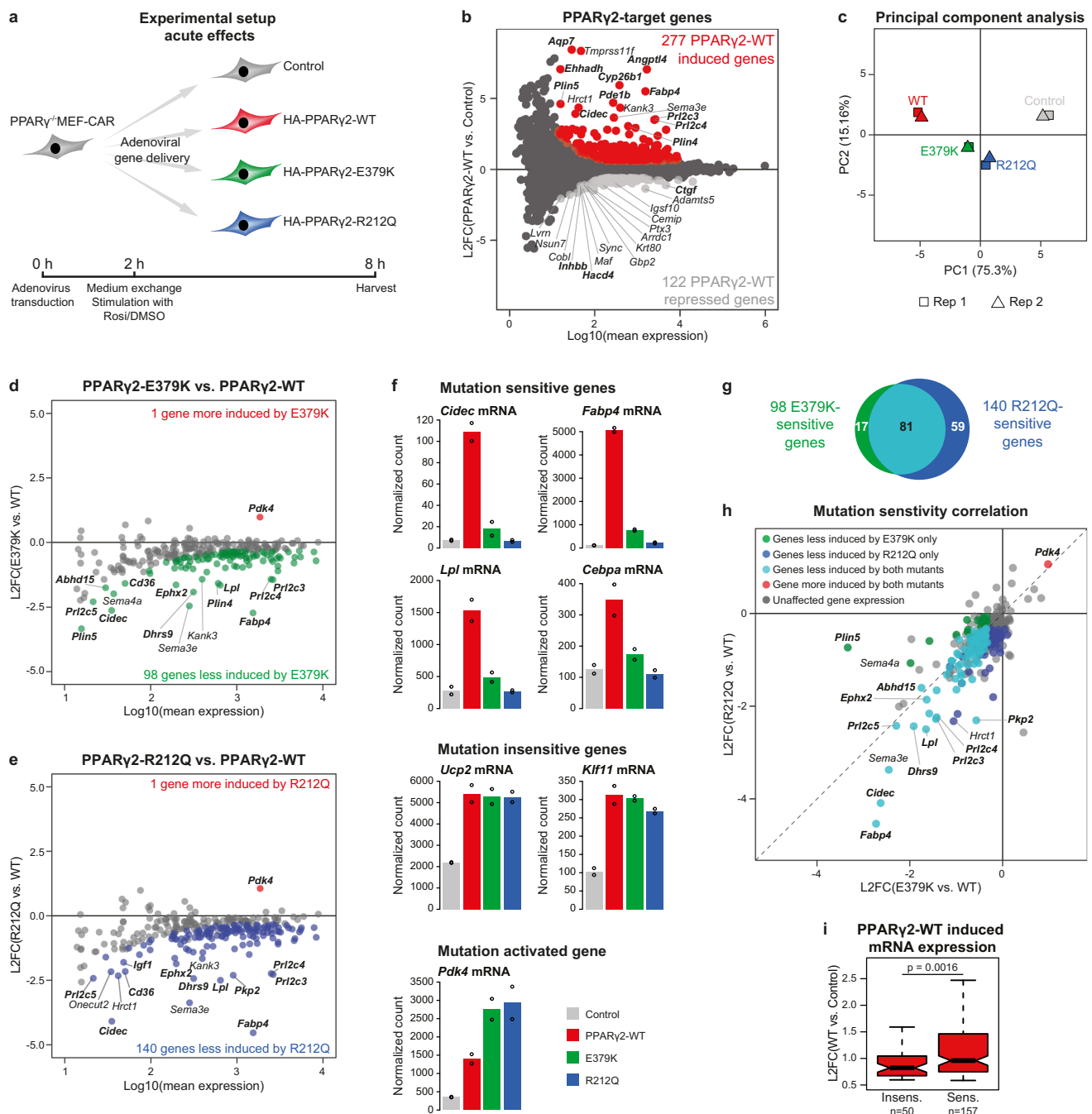


**Fig. 5 | The E379K and R212Q mutants display partial deregulation of PPAR $\gamma$ -target genes.** **a** Experimental outline showing the timing of virus transduction, ligand stimulation (1  $\mu$ M Rosiglitazone) and harvest of PPAR $\gamma$ <sup>-/-</sup> MEF-CAR cells to investigate acute transcriptional changes upon introduction of WT and mutant PPAR $\gamma$ 2s. **b** Identification of PPAR $\gamma$ 2-target genes from RNA-seq data. PPAR $\gamma$ 2-WT induced (red dots) and repressed (light gray dots) genes are defined using DESeq2 with Benjamini–Hochberg correction ( $\text{padj.} < 0.05$ , two-sided) and increasing or decreasing by a fold change  $> 1.5$  compared to control cells, respectively. Black dots represent unaffected genes. L2FC, log<sub>2</sub> fold change. Top-15 most induced and repressed genes are indicated, with genes known to be involved in adipocyte biology marked in bold. **c** Variance in RNA-seq data ( $n = 2$  independent biological experiments). Identification of **d** E379K-sensitive and **e** R212Q-sensitive PPAR $\gamma$ 2-target genes. Red dots represent genes more induced by mutant compared to WT PPAR $\gamma$ 2 ( $\text{padj.}(\text{mut vs. WT}) < 0.05$ , FC (mut vs. WT)  $> 1.25$ ). Green and blue dots represent genes less induced by E379K and R212Q compared to WT, respectively ( $\text{padj.}(\text{mut vs. WT}) < 0.05$ , FC (mut vs. WT)  $< -1.25$ ). Statistical significance was

determined by DESeq2 using Benjamini–Hochberg correction, two-sided test. L2FC, log<sub>2</sub> fold change. Top-15 less induced genes are indicated. Genes known to be involved in adipocyte biology are marked in bold. **f** Bar plots indicating RNA-seq based expression of selected PPAR $\gamma$ 2-target genes. Bars represent mean of independent biological replicates ( $n = 2$ ), dots indicate individual replicates. **g** Venn diagram representing overlap of genes that are significantly downregulated by PPAR $\gamma$ 2-E379K and -R212Q. **h** Correlation of sensitivity to the E379K and R212Q mutations relative to WT (L2FC, log<sub>2</sub> fold change). Top-10 most affected genes for each mutant vs. WT is indicated. **i** Boxplot displaying induction levels for genes affected by one or both mutations (sens.,  $n = 157$ ) or genes changing less than 25% (mutant vs. WT) (insens.,  $n = 50$ ). L2FC, log<sub>2</sub> fold change. Data are presented as notch, median; box, first and third quartiles; whiskers, 1.5 times the interquartile range. Statistical significance was determined by two-sided unpaired two-samples Wilcoxon–Mann–Whitney test. Source data for panel **b–i** are provided in the Source Data file.

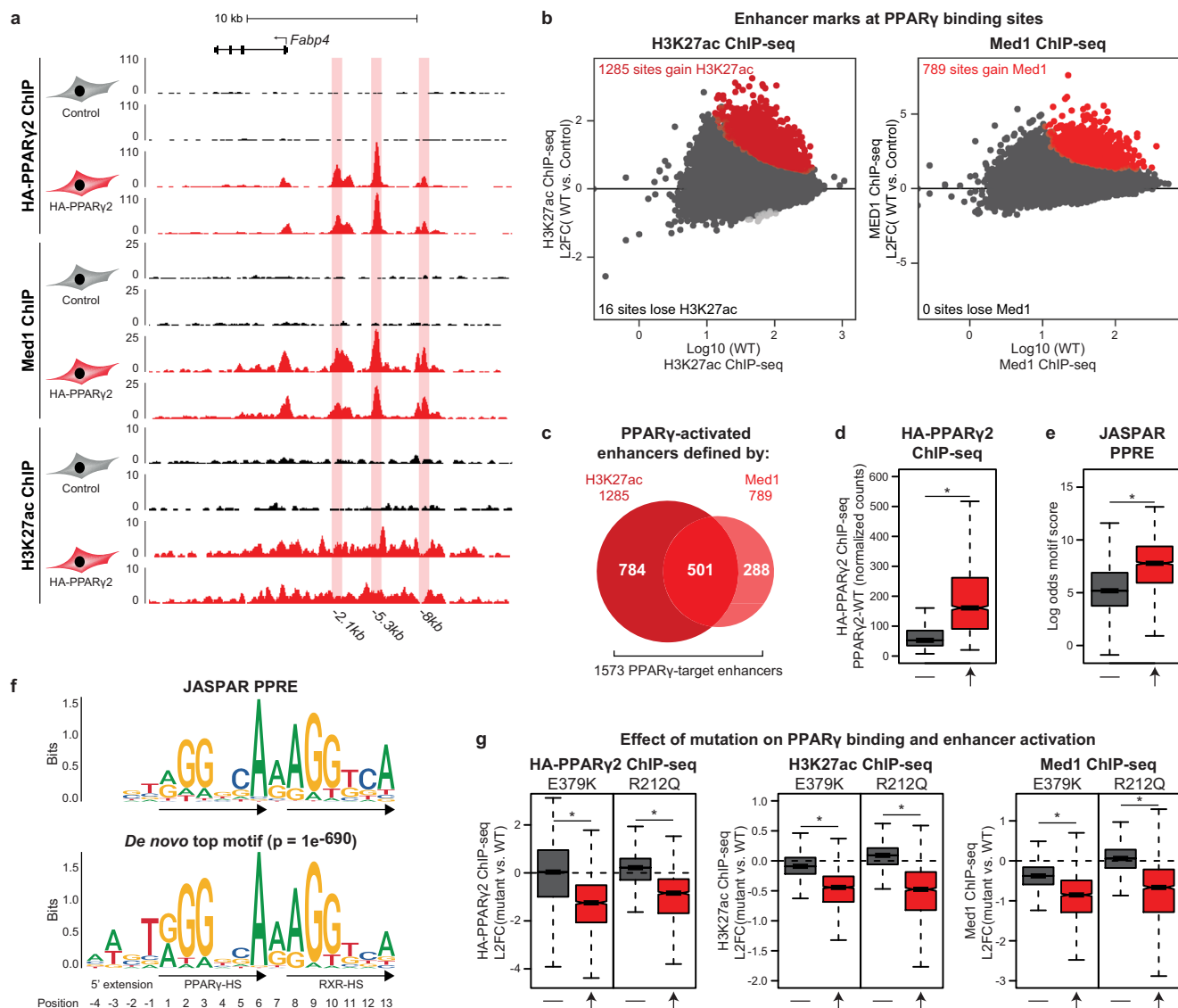


**Fig. 6 | A subset of PPAR $\gamma$ -bound sites are functional PPAR $\gamma$ -target enhancers.**

**a** UCSC Genome Browser screenshot showing HA-PPAR $\gamma$ , Med1, and H3K27ac ChIP-seq in control and PPAR $\gamma$ -WT expressing cells at the *Fabp4*-locus. PPAR $\gamma$ -binding sites (identified using Homer findPeaks and extended to 500 bp and passing a cutoff of <35 tags) are highlighted. Annotation of PPAR $\gamma$ -binding sites are relative to the transcriptional start site (TSS) of *Fabp4*. **b** Identification of enhancers activated by PPAR $\gamma$ -WT. H3K27ac and Med1 ChIP-seq signal was counted within 41830 PPAR $\gamma$  binding sites extended  $\pm 1500$  bp (H3K27ac) or  $\pm 250$  bp (Med1) from peak center. Red and light gray points indicate enhancers that gain or lose ChIP-seq signal, respectively, upon PPAR $\gamma$ -WT expression. Significance was determined by DESeq2 with Benjamini–Hochberg correction, two-sided test (FDR < 0.1). L2FC, log<sub>2</sub> fold change. **c** Venn diagram showing the number of activated enhancers defined by gain in H3K27ac and/or Med1 ChIP-seq signal, in total identifying 1573 PPAR $\gamma$ -target enhancers. **d** Boxplot of PPAR $\gamma$  ChIP-seq signal in enhancers that does not

gain or lose enhancer activity upon PPAR $\gamma$ -WT expression ( $-$ ,  $n = 40241$ ), or at PPAR $\gamma$ -target enhancers as defined in panel **b**, **c** ( $\uparrow$ ,  $n = 1573$ ). **e** JASPAR PPRE-motif score of the highest scoring motif within  $\pm 100$ bp from peak center.  $-$ : Non-activated enhancers,  $\uparrow$ : PPAR $\gamma$ -target enhancers. **f** Position weight matrix (PWM) for the JASPAR PPRE (top) and the de novo top motif (bottom). De novo motif search was made using Homer findMotifsGenome and searched within  $\pm 100$  bp of peak center of PPAR $\gamma$ -target enhancers with motif length of 15–17 bases. PPAR-HS PPAR-half site, RXR-HS RXR-half site. **g** Mutations affect primarily PPAR $\gamma$ -target enhancers. Boxplots showing the log<sub>2</sub> fold change (L2FC) (mutant vs. WT) for HA-PPAR $\gamma$ , H3K27ac, and Med1 ChIP-seq signal in non-activated ( $-$ ) and activated ( $\uparrow$ ) enhancers. For all boxplots, data are presented as notch, median; box, first and third quartiles; whiskers, 1.5 times the interquartile range.  $*p < 2e-16$  using two-sided unpaired two-samples Wilcoxon–Mann–Whitney test. Source data for panel **b**, and **d–g** are provided in the Source Data file.

### E379K and R212Q mutants affect recruitment of PPAR $\gamma$ to a subset of PPAR $\gamma$ -target enhancers

The finding that R212Q and E379K mutant proteins compromise transactivation of only a subset of target genes and that this subset is mostly shared between the mutants is intriguing and indicates that a subcategory of enhancers may be particularly sensitive to PPAR $\gamma$  mutations.

HA-PPAR $\gamma$  chromatin immunoprecipitation sequencing (ChIP-seq) of PPAR $\gamma$ <sup>-/-</sup> MEF-CAR cells transduced with adenoviral vectors expressing PPAR $\gamma$  for 2 h followed by treatment with rosiglitazone for

6 h revealed 41,830 PPAR $\gamma$ -WT binding sites (four-fold enrichment above local background,  $p < 0.0001$ ) (Fig. 6a). To evaluate the importance of PPAR $\gamma$  at these binding sites, we performed H3K27 acetylation (H3K27Ac) and Med1 ChIP-seq, which are well-established proxies for enhancer activity. Notably, for the majority of PPAR $\gamma$  binding sites, PPAR $\gamma$  recruitment is not associated with significant changes in H3K27Ac or Med1 occupancy within the time frame of the experiment (Fig. 6b). Thus, PPAR $\gamma$  recruitment leads to increased H3K27Ac at only 1285 sites and Med1 recruitment at 789 PPAR $\gamma$  binding sites (FDR < 0.1), (Fig. 6b), with 501 sites displaying an increase in both marks



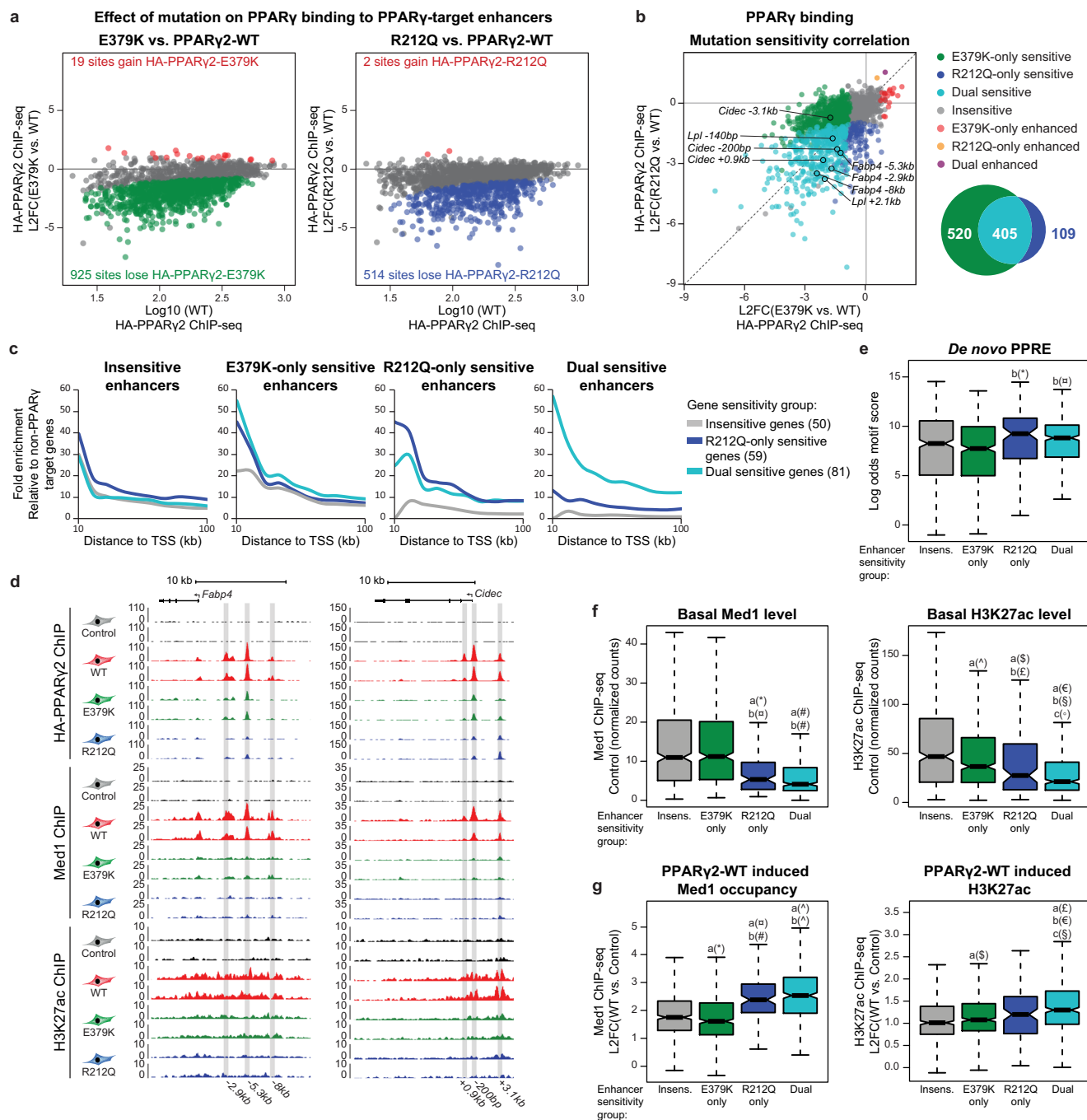


**Fig. 7 | PPAR $\gamma$  target enhancers display different sensitivity to mutations dependent on basal enhancer activity.** **a** MA-plots of PPAR $\gamma$ 2-E379K (left) and PPAR $\gamma$ 2-R212Q (right) binding relative to PPAR $\gamma$ 2-WT binding (L2FC, log<sub>2</sub> fold change). Gained and lost binding is defined by padj. (mut vs. WT) < 0.05 (DESeq2 with Benjamini–Hochberg correction, two-sided) and the binding intensity (mut vs. WT) increasing or decreasing by at least 25%, respectively. **b** Correlation of sensitivity to E379K mutation and R212Q mutation (left) (L2FC, log<sub>2</sub> fold change). Selected enhancers are indicated. Venn-diagram of enhancers with mutation-facilitated reduced PPAR $\gamma$ -binding (right). **c** Enrichment of enhancers in the vicinity of PPAR $\gamma$ -target genes relative to the number of enhancers in the vicinity of 200 randomly selected genes not regulated by PPAR $\gamma$ . R212Q-only and dual-sensitive genes are defined as in Fig. 5h. Insensitive target genes are changing less than 25% comparing mutant vs. WT PPAR $\gamma$ . E379K-only sensitive genes are excluded from the analysis as the gene group is very small (17 genes). (TSS, transcriptional start site). **d** UCSC Genome Browser track showing HA-PPAR $\gamma$ , Med1, and H3K27ac ChIP-seq at the *Fabp4*-locus (left) and *Cidec*-locus (right). PPAR $\gamma$ -target enhancers are

highlighted. **e** Boxplot of log odds motif score for the de novo PPRE within groups of enhancers. Significance was assessed by two-sided pairwise Wilcoxon rank sum tests with Benjamini–Hochberg correction, **a**, versus insensitive enhancer group (insens.,  $n = 519$ ); **b**, versus E379K-only sensitive enhancer group ( $n = 520$ ); **c**, versus R212Q-only sensitive enhancer group ( $n = 109$ ); dual-sensitive group ( $n = 405$ ),  $^*p = 0.0005$ ,  $^{\#}p = 5.7e-5$ . **f** Boxplot of basal Med1 (left) and H3K27ac (right) ChIP-seq signal within enhancer groups. Significance was assessed as in panel **e**.  $^*p = 4.8e-10$ ,  $^{\#}p = 3.3e-10$ ,  $^{\#}p < 2e-16$ ,  $^{\$}p = 0.0030$ ,  $^{\$}p = 0.00062$ ,  $^{\epsilon}p = 0.024$ ,  $^{\rho}p < 2e-16$ ,  $^{\rho}p = 2.4e-14$ ,  $^{\rho}p = 0.046$ . **g** Boxplot of PPAR $\gamma$ 2-WT induced changes in Med1 and H3K27ac ChIP-seq signal within enhancer groups (L2FC, log<sub>2</sub> fold change). Significance was assessed as in panel **e**.  $^*p = 0.0037$ ,  $^{\#}p = 1.4e-11$ ,  $^{\#}p = 4.3e-16$ ,  $^{\rho}p < 2e-16$ ,  $^{\rho}p = 0.024$ ,  $^{\epsilon}p = 9.4e-12$ ,  $^{\epsilon}p = 1.1e-7$ ,  $^{\rho}p = 0.049$ . Data in boxplots are presented as notch, median; box, first and third quartiles; whiskers, 1.5 times the interquartile range. Source data for panel **a–c** and **e–f** are provided as a Source Data file.

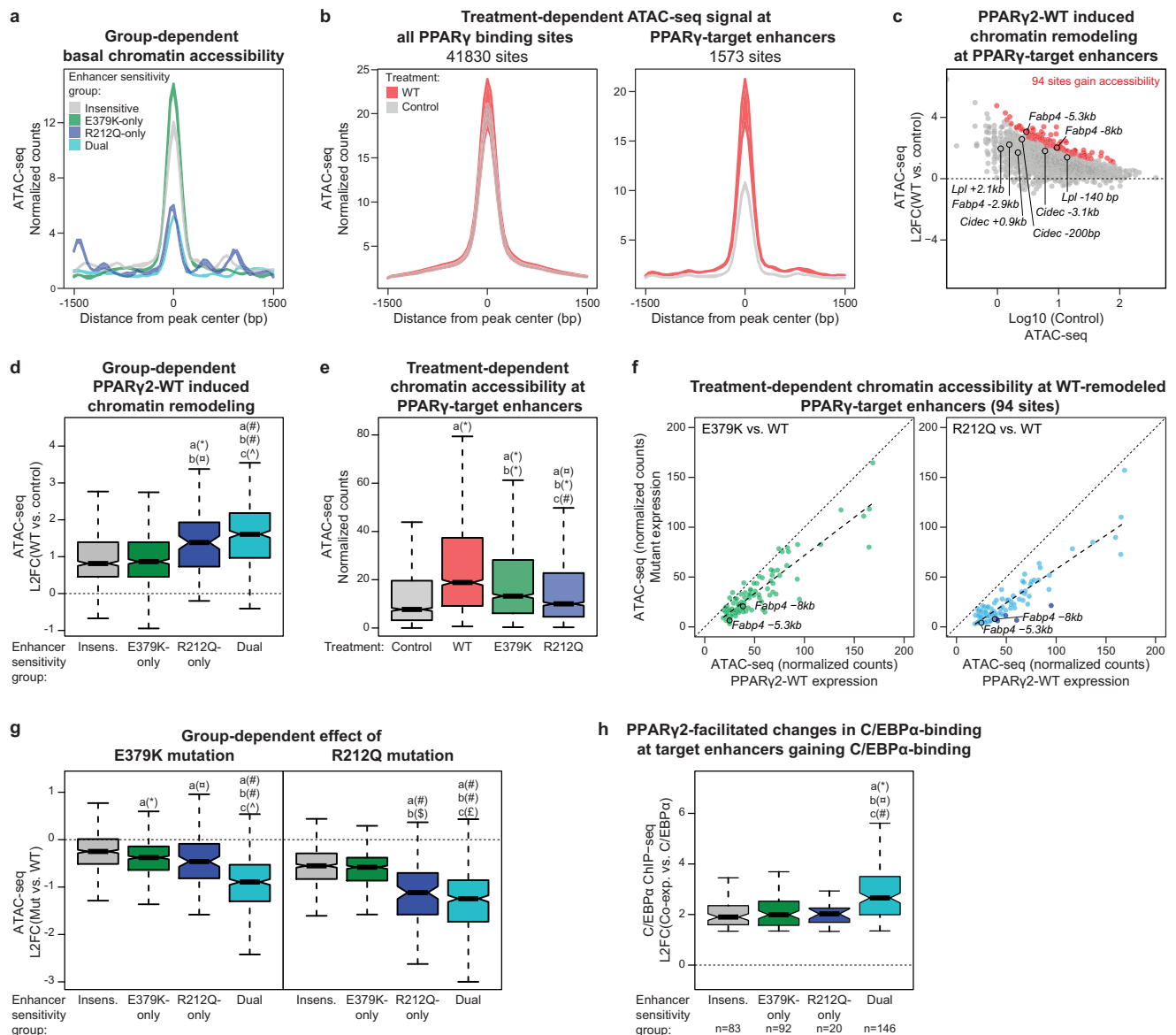


**Fig. 8 | R212Q-sensitive enhancers are found in less accessible regions of the chromatin.** **a** Enhancer group-dependent ATAC-seq signal in control cells. Colored area represents the difference between the two replicates. **b** Treatment-dependent ATAC-seq signal from control and PPAR $\gamma$ 2-WT expressing PPAR $\gamma$ <sup>-/-</sup> MEF-CAR cells on all PPAR $\gamma$  binding sites (left) or PPAR $\gamma$ -target enhancers (right). Colored area represents the difference between the two replicates. **c** MA-plot of PPAR $\gamma$ 2-WT induced chromatin accessibility at PPAR $\gamma$ -target enhancers (L2FC, log<sub>2</sub> fold change). Gained accessibility is defined using DESeq2 with Benjamini–Hochberg correction, two-sided test, padj < 0.05, L2FC(WT vs. control) > 0. Selected enhancers are indicated. **d** Enhancer group-dependent PPAR $\gamma$ 2-WT induced chromatin remodeling. Significance was assessed by two-sided pairwise Wilcoxon rank sum tests with Benjamini–Hochberg correction, a, versus insensitive enhancer group (n = 519); b, versus E379K-only sensitive enhancer group (n = 520); c, versus R212Q-only sensitive enhancer group (n = 109), dual-sensitive enhancer group (n = 405), \*p = 1.7e-7, #p = 4.7e-7, #p < 2e-16, #p = 0.01. **e** Treatment-dependent ATAC-seq signal at PPAR $\gamma$ -target enhancers (n = 1573). Significance was assessed by two-sided

pairwise Wilcoxon rank sum tests with Benjamini–Hochberg correction, a, versus control; b, versus WT expression; c, versus E379K-expression, \*p < 2e-16, #p = 2.3e-9, #p = 6.8e-9. **f** ATAC-seq signal of E379K (left) and R212Q (right) treated cells relative to the WT ATAC-seq signal at enhancers where PPAR $\gamma$ 2-WT significantly induces remodeling (94 sites defined in panel c). Linear models fitting the data are indicated with dashed lines. Enhancers that significantly lose ATAC-seq signal upon R212Q mutation are marked with dark blue (DESeq2 with Benjamini–Hochberg correction, two-sided test, padj < 0.05, L2FC(R212Q vs. WT) < 0). Selected enhancers are indicated. **g** Mutation-induced changes in remodeling capacity within enhancer groups. Significance was assessed as in panel d. \*p = 1.2e-6, #p = 0.00027, #p < 2e-16, #p = 1.9e-11, #p = 8e-16, #p = 0.043. **h** Enhancer group-dependent PPAR $\gamma$ 2-induced gain in C/EBP $\alpha$  ChIP-seq signal upon PPAR $\gamma$ 2 and C/EBP $\alpha$  co-expression in PPAR $\gamma$ <sup>-/-</sup> MEF-CAR cells. Data from Madsen et al.<sup>6</sup>. Significance was assessed as in panel d. \*p = 2.2e-6, #p = 1.7e-6, #p = 0.0014. Data in boxplots are presented as notch, median; box, first and third quartiles; whiskers, 1.5 times the interquartile range. Source data are provided in the Source Data file.

(Fig. 6c). Based on this, we defined ‘PPAR $\gamma$ -target enhancers’ as the 1573 putative enhancers that gain H3K27ac and/or Med1 in response to PPAR $\gamma$  binding. Importantly, PPAR $\gamma$ -target enhancers display higher average PPAR $\gamma$  occupancy and a stronger PPRE motif, compared with the other binding sites (Fig. 6d, e), and the top-scoring de novo motif found within PPAR $\gamma$ -target enhancers resembles the JASPAR PPRE (Fig. 6f). Taken together, this indicates that PPAR $\gamma$ -activated sites are

functional PPAR $\gamma$  binding sites, where PPAR $\gamma$  acts as a key driver of enhancer activity.

To investigate how the E379K and R212Q mutations affect the ability of PPAR $\gamma$  to bind to chromatin and activate enhancers, we repeated the PPAR $\gamma$ , H3K27ac, and MED1 ChIP-seq for the PPAR $\gamma$  mutants. Interestingly, the mutations did not affect overall PPAR $\gamma$  association with chromatin but selectively compromised PPAR $\gamma$

binding and enhancer activation at PPAR $\gamma$ -target enhancers (Fig. 6g). Taken together, these results indicate that only a small subset of PPAR $\gamma$  binding sites are functionally important PPAR $\gamma$ -target enhancers, and that PPAR $\gamma$  recruitment to these on average is sensitive to mutations that destabilize the PPAR $\gamma$ :RXR heterodimer binding to DNA.

To better understand how the two mutations affect the recruitment of PPAR $\gamma$  to target enhancers, we analyzed how mutations affect the binding of PPAR $\gamma$  to each of the PPAR $\gamma$ -target enhancers. Out of the 1573 target enhancers (Fig. 6c), E379K decreased binding to 925 enhancers, while R212Q decreased binding to 514 enhancers (Fig. 7a). Interestingly, the reduced ability of the mutant PPAR $\gamma$  proteins to engage with chromatin defines clear subclasses of enhancers, where 405 enhancers display reduced binding of both mutants, whereas 520 and 109 enhancers are selectively less bound by E379K and R212Q, respectively (Fig. 7b). Dual-sensitive enhancers are highly enriched in the vicinity of dual and R212Q-only sensitive genes compared to insensitive genes, and R212Q-only sensitive enhancers are more often found in the vicinity of dual and R212Q-only sensitive genes (Fig. 7c). These findings indicate that the decreased binding of the mutants to target enhancers is functionally linked to their reduced activation potential. For instance, binding of PPAR $\gamma$  to the well-known PPRES controlling expression of the mutation-sensitive genes *Fabp4*<sup>29</sup>, *Cidec*<sup>19</sup>, and *Lpl*<sup>18</sup> is compromised by the mutations, while binding of PPAR $\gamma$  to the *Ucp3* intronic PPRES controlling expression of the mutation-insensitive gene *Ucp2*<sup>25</sup> is unaffected by the mutations (Fig. 7d and Supplementary Fig. 6).

Functional characterization of the different subclasses of enhancers showed that enhancers that primarily are sensitive to R212Q (R212Q-only) are characterized by strong PPRES motifs (Fig. 7e), low levels of enhancer activity in the non-transduced cells (Fig. 7f) and a high fold increase in enhancer activity (Med1 recruitment) in response to PPAR $\gamma$ -WT (Fig. 7g). This indicates that these represent enhancers that are highly dependent on PPAR $\gamma$  for activation. In contrast, enhancers primarily sensitive to E379K are characterized by a weaker PPRES (Fig. 7e), high levels of enhancer activity in the non-transduced cells (Fig. 7f), and less fold increase in Med1 recruitment in response to PPAR $\gamma$ -WT, indicating that these are enhancers where PPAR $\gamma$  plays a more modest role. The enhancers that are sensitive to both mutations generally share many characteristics of the R212Q-only enhancers, including strong PPRES motifs (Fig. 7e) and dependency on PPAR $\gamma$  for activation (Fig. 7f, g). Finally, PPAR $\gamma$ -target enhancers that are insensitive to mutations are more similar to E379K by having high levels of enhancer activity in the absence of PPAR $\gamma$  (Fig. 7f) and by being more modestly activated by PPAR $\gamma$  (Fig. 7g). Consistent with that, receiver-operating characteristic (ROC) analysis indicates that activity of the PPAR $\gamma$ -target enhancer in the non-transduced cells is the best predictor of mutation sensitivity (Supplementary Fig. 7).

Taken together, PPAR $\gamma$ -target enhancers with low activity in the absence of PPAR $\gamma$  are, on average sensitive to both mutations, especially the R212Q mutation, whereas PPAR $\gamma$ -target enhancers, which are already active prior to expression of PPAR $\gamma$  are primarily sensitive to the E379K mutation.

### E379K and R212Q mutants decrease the remodeling capacity of PPAR $\gamma$

Local chromatin structure constitutes a major determinant of the ability of transcription factors to bind to DNA<sup>30</sup>, and we hypothesized that chromatin accessibility could discriminate between mutation-sensitive and insensitive-sites. We therefore determined chromatin accessibility in non-transduced PPAR $\gamma$ <sup>-/-</sup> MEF-CARs using an assay for transposase-accessible chromatin sequencing (ATAC-seq). Notably, examination of a 3 kb window centered around the PPAR $\gamma$  peak shows that R212Q-only and dual-sensitive PPAR $\gamma$ -target enhancers have low chromatin accessibility (i.e., are nucleosome-rich) in chromatin prior to expression of PPAR $\gamma$ , whereas insensitive and E379K-only sensitive

enhancers are already accessible in non-transduced cells (Fig. 8a and Supplementary Fig. 8). These findings are consistent with the notion that the R212Q-sensitive enhancers are inactive in the non-transduced state and highly dependent on PPAR $\gamma$  for activation.

To examine the ability of PPAR $\gamma$  to drive the remodeling of target enhancers, we assessed chromatin accessibility before and after transduction with Ad-mPPAR $\gamma$ 2-WT. Whereas PPAR $\gamma$  expression does not affect average chromatin accessibility at all PPAR $\gamma$  binding sites, it specifically increases chromatin accessibility at PPAR $\gamma$ -target enhancers, with 94 enhancers significantly gaining accessibility (FDR < 0.05) by ATAC-seq (Fig. 8b, c). Notably, R212Q-sensitive enhancers gain more accessibility than insensitive and E379K-only enhancers (Fig. 8d), consistent with the higher gain in activity at these enhancers (Fig. 7g).

The finding that R212Q-sensitive enhancers are relatively inaccessible and inactive prior to expression of PPAR $\gamma$  indicates that the R212 residue, possibly through its direct interaction with the minor groove in DNA<sup>11-13</sup>, is important for the ability of PPAR $\gamma$  to bind to and remodel inactive PPAR $\gamma$ -target enhancers. To directly assess this, we compared the ability of PPAR $\gamma$ -WT and the R212Q and E379K mutants to remodel target enhancers. While both mutations significantly diminish PPAR $\gamma$ -induced remodeling, the R212Q mutation has the most dramatic effect (Fig. 8e, f). Intriguingly, however, the R212Q mutation also leads to slightly decreased remodeling and activation of target enhancers, where PPAR $\gamma$  binding is not affected by the mutation (insensitive and E379K-only enhancers) (Fig. 8g and Supplementary Fig. 9). Taken together, these findings indicate that the R212Q mutation in PPAR $\gamma$  compromises the ability to bind to enhancers in closed chromatin and induce the remodeling and activation of these enhancers, but that the mutation also affects the activation of enhancers independent of the level of PPAR $\gamma$  binding. Similarly, the E379K mutation affects the remodeling and activation of R212Q-only enhancers (Fig. 8g and Supplementary Fig. 9), suggesting that this mutation also modestly affects the activation of enhancers independent of PPAR $\gamma$  binding.

We have previously shown that the two adipocyte master regulators, PPAR $\gamma$  and C/EBP $\alpha$ , can potentiate the binding of each other to shared binding sites in closed chromatin in PPAR $\gamma$ <sup>-/-</sup> MEF-CAR cells<sup>6</sup>. Of interest to this work, we showed that the ability of PPAR $\gamma$ 2 to act as a leading factor facilitating C/EBP $\alpha$  binding appeared to be dependent on a strong PPRES, indicating that PPAR $\gamma$  requires a strong PPRES to bind to DNA in nucleosome-embedded chromatin. Interestingly, by comparing these data with the current study, we found that dual-sensitive PPAR $\gamma$  target enhancers, which are 1) most inactive in the absence of PPAR $\gamma$  (Fig. 7f); 2) most sensitive to PPAR $\gamma$ -induced remodeling (Fig. 8d); and 3) most sensitive to PPAR $\gamma$  mutations (Fig. 8g), generally are enhancers where PPAR $\gamma$  act as the leading factor for C/EBP $\alpha$  (Fig. 8h).

### R212Q-sensitive enhancers contain PPRESs with consensus 5'-extension

Since our data indicated that R212 in PPAR $\gamma$  is important for the recruitment of PPAR $\gamma$  to closed chromatin, we dissected the PPRES motif into the 5' extension, the PPAR $\gamma$  half site, and the RXR-half site (Fig. 6f) and assessed the motif score within each of these segments for the different subgroups of PPAR $\gamma$ -target enhancers (Fig. 9a). Interestingly, the 5' extension, as well as the PPAR $\gamma$  half site, has a higher motif score in R212Q-sensitive enhancers compared to E379K-only and insensitive target enhancers.

To further investigate the importance of the PPRES-motif strength, we classified PPAR $\gamma$ -target enhancers as open or closed based on their basal accessibility and assessed the effect of mutations on PPAR $\gamma$  binding for different intervals of PPRES-motif score (Fig. 9b). This shows that when the target enhancer is in accessible chromatin, WT PPAR $\gamma$  and both E379K and R212Q mutants are recruited equally well to PPRESs with high motif strength (>12),

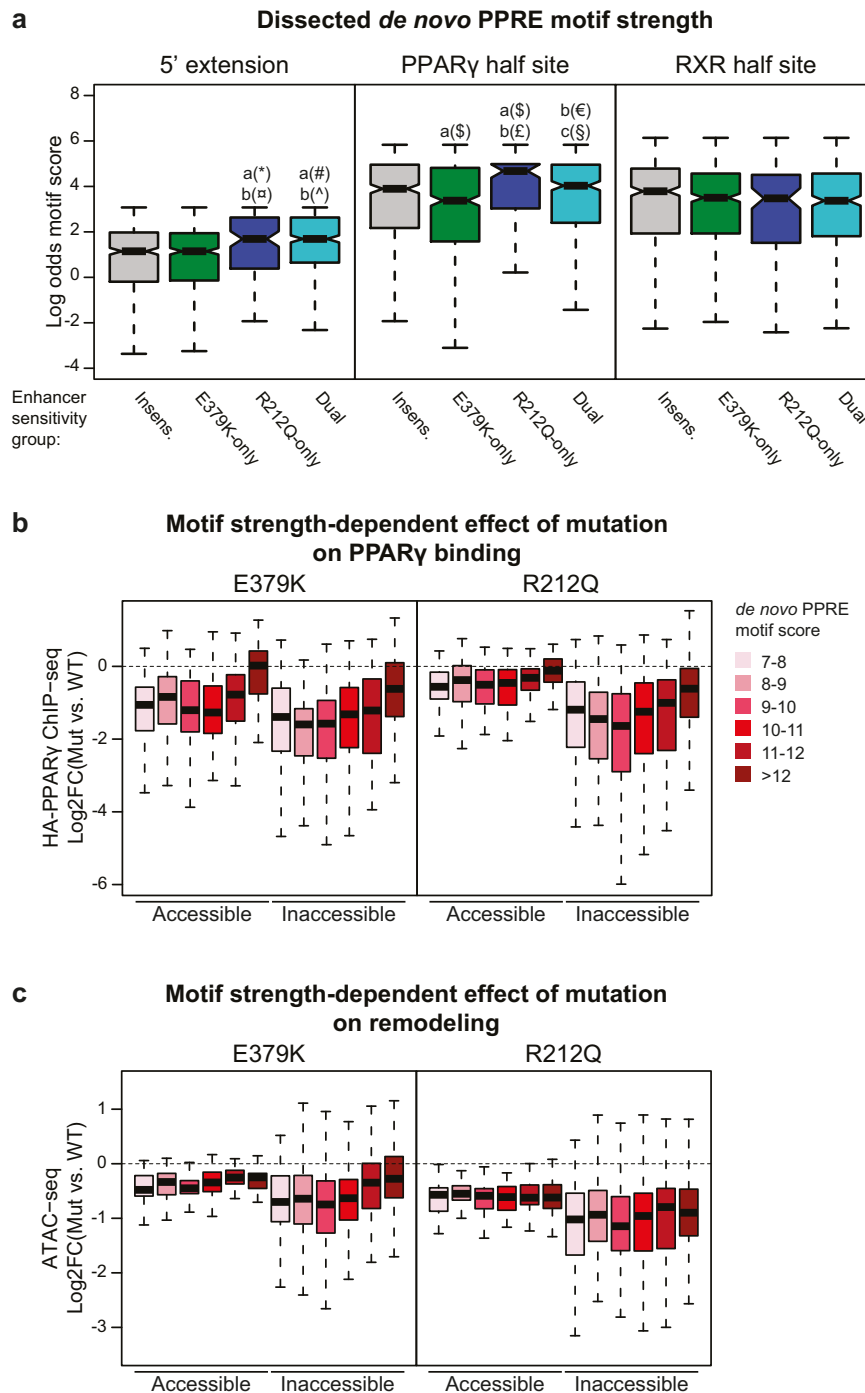


**Fig. 9 | R212Q-sensitive enhancers are characterized by a stronger 5'-extension and PPAR $\gamma$ -half site.** **a** The *de novo* PPRE (Fig. 6f) was dissected into the 5' extension, PPAR $\gamma$ -half site, and RXR-half site and the motif strength was assessed within these sections for each group of enhancers. Significance was assessed by two-sided pairwise Wilcoxon rank sum tests with Benjamini–Hochberg correction, **a**, versus insensitive enhancer group ( $n = 519$ ); **b**, versus E379K-only sensitive enhancer group ( $n = 520$ ); **c**, versus R212Q-only sensitive enhancer group ( $n = 109$ ), dual-sensitive enhancer group ( $n = 405$ ), \* $p = 0.00022$ , <sup>a</sup> $p = 5.8e-5$ , <sup>#</sup> $p = 5.7e-10$ , <sup>†</sup> $p = 8.1e-12$ , <sup>§</sup> $p = 0.0052$ , <sup>‡</sup> $p = 2e-5$ , <sup>¶</sup> $p = 0.0037$ , <sup>§</sup> $p = 0.011$ . Boxplots are presented as notch, median; box, first and third quartiles; whiskers, 1.5 times the interquartile range.

**b, c** PPAR $\gamma$ -target enhancers were divided into accessible (normalized counts > 15 tags) and inaccessible (normalized counts < 15 tags) enhancers based on the ATAC-seq data. The effect of mutation on **b** PPAR $\gamma$  binding and **c** ATAC-seq signal was assayed dependent on the PPRE-motif strength within the PPAR $\gamma$ -target enhancer. Accessible enhancers:  $n_{\text{Motif score } 7-8} = 53$ ;  $n_{\text{Motif score } 8-9} = 53$ ;  $n_{\text{Motif score } 9-10} = 63$ ;  $n_{\text{Motif score } 10-11} = 55$ ;  $n_{\text{Motif score } 11-12} = 26$ ;  $n_{\text{Motif score } >12} = 27$ . Inaccessible enhancers:  $n_{\text{Motif score } 7-8} = 92$ ;  $n_{\text{Motif score } 8-9} = 129$ ;  $n_{\text{Motif score } 9-10} = 142$ ;  $n_{\text{Motif score } 10-11} = 176$ ;  $n_{\text{Motif score } 11-12} = 92$ ;  $n_{\text{Motif score } >12} = 95$ . Boxplots are presented as bold line, median; box, first and third quartiles; whiskers, 1.5 times the interquartile range. Source data are provided in the Source Data file.

whereas recruitment is negatively affected by the E379K mutation but not the R212Q mutation when the motif score is decreasing. Importantly, for target enhancers in inaccessible chromatin, the ability of both mutants to bind to target enhancers is highly dependent on the motif strength.

Taken together, these results show that the R212 residue is important for the ability of PPAR $\gamma$  to recruit to sites in closed chromatin, whereas the binding to nucleosome-free accessible target sites is much less affected by this mutation. Interestingly, however, the remodeling capacity of PPAR $\gamma$ -R212Q is compromised independently

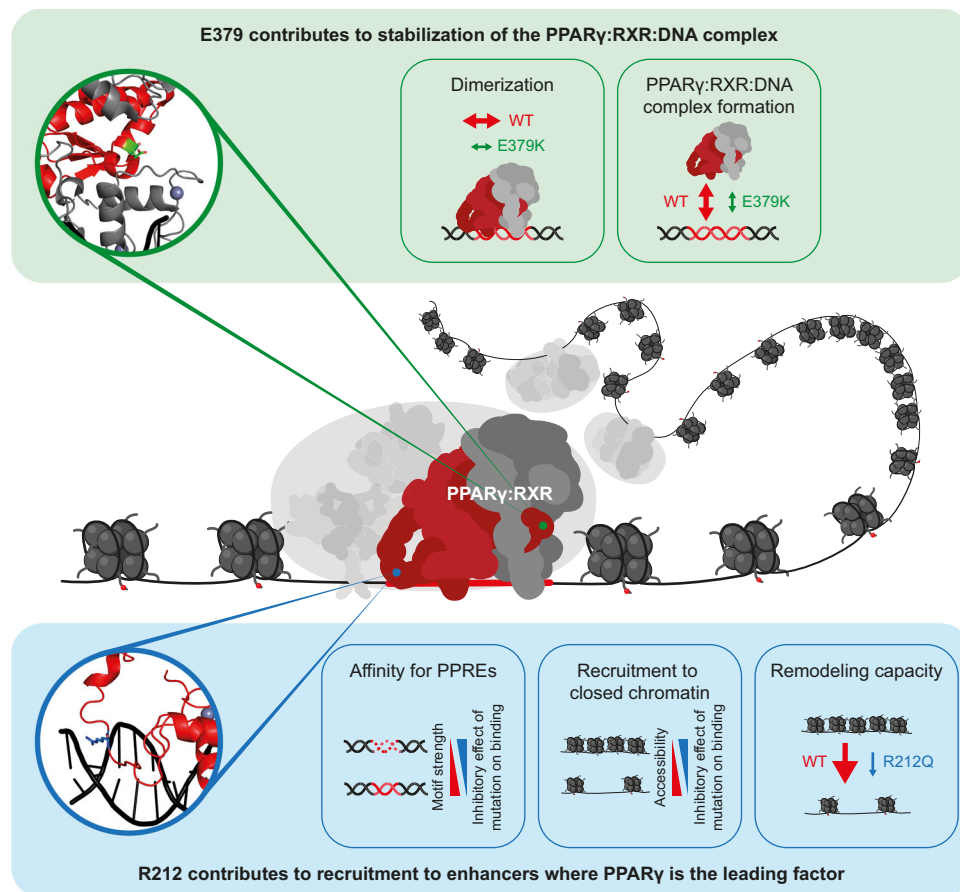


**Fig. 10 | Model illustrating how E379K and R212Q lipodystrophy mutants reveal important interaction interfaces in the PPAR $\gamma$ :RXR:DNA complex.** Central panel: PPAR $\gamma$ :RXR:DNA ternary complex with the respective positions of E379 and

R212 residues based on the crystal structure<sup>11</sup>. Top panel: the molecular effect of the E379K mutation. Lower panel: the molecular effect of the R212Q mutant. See text for further explanation.

of motif score and PPAR $\gamma$  recruitment, suggesting that PPAR $\gamma$ -R212 is particularly important for the ability of PPAR $\gamma$  to remodel chromatin (Fig. 9c). The E379K mutation also displays the greatest effect on PPAR $\gamma$  binding to inaccessible sites; however, in addition, it decreases binding of PPAR $\gamma$  to accessible target sites in a motif-strength-dependent manner. This suggests that the motif becomes more important for the formation of the ternary PPAR $\gamma$ :RXR:DNA complex when the PPAR $\gamma$ :RXR heterodimer is destabilized by the E379K mutation. Collectively, these data reveal novel mechanisms contributing to the stabilization of the binding of the PPAR $\gamma$ :RXR dimer to DNA, which is particularly important in enhancers where PPAR $\gamma$  acts as the leading factor.

## Discussion

Structure-based studies have indicated extensive intermolecular interactions in the DNA-bound PPAR $\gamma$ :RXR heterodimer<sup>11–13</sup>, but how these interactions translate into gene activation in a cellular context, i.e. in cooperation with other transcription factors and in the context of chromatin, is currently poorly understood. Here we employed two previously uncharacterized FPLD3-associated PPAR $\gamma$  mutants, predicted to be involved in intermolecular interactions in the PPAR $\gamma$ :RXR:DNA complex, to probe the molecular mechanisms underlying enhancer activation by PPAR $\gamma$ . We show that the R212Q and E379K mutations in PPAR $\gamma$  lead to reduced adipogenic potential and impaired activation of a subset of PPAR $\gamma$  target genes. Consistent with this, genome-wide analyses of the transcriptional and epigenomic properties of the mutants demonstrate that the mutations only affect the activation of a subset of PPAR $\gamma$ -target enhancers and that a major determinant of sensitivity to these mutations is low chromatin

accessibility. Interestingly, we show that the two mutations affect enhancer activity by distinct mechanisms, thereby providing insight into how PPAR $\gamma$  engages with its target sites. Furthermore, as important intra- and intermolecular interactions have been reported in other nuclear receptors (e.g. RAR $\beta$ <sup>9</sup> and GR<sup>31</sup>), it will be of interest to investigate whether disease-causing mutations in nuclear receptors other than PPAR $\gamma$  have similar effects<sup>32</sup>.

Based on the crystal structure, the R212Q mutation is expected to decrease the ability of the PPAR $\gamma$  hinge to engage in interactions within the minor groove of the DNA helix immediately 5' of the PPRE (referred to as the 5' extension or 5' upstream region; 5' UR)<sup>11</sup>. Previous studies based on selected target sites indicated that the 5' extension is required for PPAR:RXR binding to suboptimal direct repeats and that this sequence provides specificity of the PPRE towards the PPAR:RXR heterodimer<sup>33,34</sup>. Consistent with a role for the interaction between the PPAR $\gamma$  hinge and the 5' extension of the PPRE in chromatin, genome-wide profiling of PPAR $\gamma$  occupancy by ChIP-seq has shown that the 5' extension is enriched in natural PPAR $\gamma$ :RXR binding sites<sup>3,4,6</sup>. Here we show that the R212Q mutation interferes with the ability of PPAR $\gamma$  to recruit to and remodel target sites in nucleosome-rich chromatin, whereas there is little effect on binding to accessible nucleosome-free target sites. This indicates that the interaction between the PPAR $\gamma$  hinge and the 5' extension of the PPRE is particularly important for the ability of PPAR $\gamma$  to bind to target sites in nucleosome-rich chromatin. In addition, this interaction appears to enhance chromatin remodeling capacity independent of PPAR $\gamma$  binding, possibly by increasing intermolecular interactions in the PPAR:RXR:co-factor complex, or by interfering with the interaction between DNA and nucleosomes.

According to crystallography and SAXS studies, the E379 residue is located in the LBD at a position that contacts the DBD of RXR $\alpha$  in the DNA-bound heterodimer<sup>11,14</sup>. The existence of the PPAR $\gamma$  LBD-RXR $\alpha$  DBD heterodimerization interface is a topic of debate as this interface could not be observed in solution by SAXS<sup>12,13</sup>. However, our double charge reversal mutation assay, combining the E379K mutant with RXR $\alpha$ -K175E on the *Lpl* -140bp PPRE, suggests that this interface contributes to PPAR $\gamma$ -mediated transcriptional activity. Interestingly, another recently identified variant in the *PPARG* locus giving rise to a S383R mutant PPAR $\gamma$ <sup>35</sup> is predicted to affect the same interaction interface; however, no functional data are available yet. Like the R212Q mutation, the E379K mutation has the greatest impact on the binding of PPAR $\gamma$  to inaccessible target sites in chromatin. However, this mutation also affects binding to accessible sites, indicating that this mutation leads to a more general destabilization of the PPAR $\gamma$ :RXR heterodimer. This is consistent with the observation that the E379K mutation affects PPAR $\gamma$  binding to more target enhancers than the R212Q mutation.

The finding that the R212Q mutation has the greatest effect on enhancer activity and target gene expression compared with the E379K mutation despite affecting PPAR $\gamma$  recruitment to fewer enhancers is intriguing. Most likely, this is due to the fact that the R212Q mutation leads to a more dramatic loss of remodeling capacity at target sites, including dual-sensitive target sites. Thus, whereas the E379K mutation affects PPAR $\gamma$  binding to many enhancers through destabilization of the PPAR $\gamma$ :RXR heterodimer, the R212Q mutation more severely compromises the ability of PPAR $\gamma$  to act as a facilitating transcription factor driving remodeling (Fig. 10). Since the need for PPAR $\gamma$  to act as a leading transcription factor is highly dependent on which other transcription factors are expressed, one would expect that the phenotypic result of the R212Q mutant is highly context-dependent.

Taken together, our comprehensive investigations of the functional and biochemical properties of two PPAR $\gamma$  FPLD3-associated mutants highlight the importance of intermolecular interactions for transcriptional activation. Our data indicate that the interaction between the hinge region of PPAR $\gamma$  and the 5' extension of the PPRE is particularly important for the ability of PPAR $\gamma$  to bind to and remodel enhancers in inaccessible chromatin. Furthermore, our data support the existence of a functional interface between the RXR-DBD and helix 6 in the LBD of PPAR $\gamma$  and indicate that this interaction plays a role in the general stabilization of the PPAR $\gamma$ :RXR:DNA ternary complex. Overall, this work underscores the importance of intermolecular interactions in PPAR $\gamma$  functions and indicates that the subtle molecular defects in these interactions are sufficient to cause FPLD3.

## Methods

The study was conducted according to the 1964 declaration of Helsinki and its later amendments or compatible ethical standards. The study was approved by the Ethics Committee of University Hospitals Leuven (File S57866) and the Ethics Committee NedMec (File 22–891). Written informed consent for study participation and publication was obtained from the index patients.

## Index subjects and DNA sequence analysis

Both index patient 1 and 2 displayed typical features of partial lipodystrophy: a clear excess of subcutaneous fat on the face, neck, trunk, and abdomen with a lack of subcutaneous fat on the extremities. Additional clinical features are indicated in Fig. 1a, b. Genomic DNA was extracted from peripheral-blood leukocytes in venous blood samples using QIAamp DNA Blood Mini Kit according to the manufacturer's instructions (Qiagen Hilden, Germany). We

sequenced all coding exons of *PPARG*, *AKT2*, *CIDEA*, and *LMNA* (exon 8–9), including intron-exon boundaries of the index patients. Primers are available upon request. In index patient 1 we identified a heterozygous mutation in exon 6 of the *PPARG* gene corresponding to c.1135 G > A and p.E379K in reference sequences NM\_015869 and NP\_056953.2, respectively. This variant is absent in the variation databases NHLBI GO Exome sequencing Project (ESP) (Exome Variant Server), 1000Genomes (Consortium, 2015), Single Nucleotide Polymorphism Database (dbSNP)<sup>36</sup>, and The Genome Aggregation Database (gnomAD)<sup>37</sup>. Amplification and Sanger sequencing of exon 6 and flanking regions were performed to genotype family members. In index patient 2, we identified a heterozygous mutation in exon 5 of *PPARG* corresponding to c.635 G > A and p.R212Q in reference sequences NM\_015869 and NP\_056953.2, respectively. Genotype data from family members were not available. The same variant was previously reported independently in a female subject with FPLD3 but not functionally characterized<sup>16</sup>.

## Cell culture

The murine PPAR $\gamma$ <sup>-/-</sup> MEF-CAR cell line<sup>6</sup>, human osteosarcoma cell line U2OS, and the human embryonic kidney cell line HEK293T were maintained in Dulbecco's modified Eagle's medium (DMEM; Gibco) 4.5 g/L D-glucose supplemented with 10% fetal bovine serum (Gibco), and 100  $\mu$ g penicillin/ml and 100  $\mu$ g streptomycin/ml (Invitrogen).

## Luciferase-based reporter assays

The pGL3-*mLpl*-PPRE-Luc2 (lipoprotein lipase; *Lpl*) reporter construct was generated by the insertion of one copy of the mouse *Lpl* -160 bp PPRE<sup>18</sup> upstream of the minimal promoter and one copy downstream of the luciferase gene in a pGL3-minimal promoter-luciferase 2 (Luc2) backbone (Supplementary Fig. 2)<sup>38</sup>. The pGL3-*mLpl*-PPRE-Luc2 was used as a template to generate *Lpl* 5' upstream region (5' UR) mutant, *Cidec* and Synthetic PPRE reporters using QuickChange mutagenesis kit (Stratagene) following the instructions provided by the manufacturer. The *Cidec* 5'UR mutant reporter was generated in the same way, based on the *Cidec* reporter. Primer sequences are given in Supplementary Table 1. The reporter construct 5xGal4-E1BTATA-pGL3 has previously been described<sup>39</sup>. The *Cidec* (promoter)-pGL3 luciferase reporter<sup>40</sup> was a kind gift of Dr. P.F. Marrero. pCDNA3.1 expression vectors for hPPAR $\gamma$ 2 and hRXR $\alpha$ <sup>17</sup> were used to generate the hPPAR $\gamma$ 2 mutants E379K, R212Q and R212W and the hRXR $\alpha$  K175E mutant, respectively, using the QuickChange mutagenesis kit (Stratagene). Gal4DBD-hPPAR $\gamma$ -AF2 WT, pGEX-PPAR $\gamma$ -LBD WT, pGEX-RXR $\alpha$ , pGEX-SMRT, and pGEX-SRC1 have been described previously<sup>17,41</sup> and mutants thereof were generated as described above.

For luciferase reporter assays U2OS and HEK293T cells were seeded in 24-wells plates and transiently transfected using PEI. Each well was cotransfected with a reporter construct (1  $\mu$ g), 2 ng Renilla, and PPAR and/or expression constructs (10 ng). The next day, media were removed and fresh media were added with or without 1  $\mu$ M Rosiglitazone, as indicated in the figure legends. After incubation, cells were washed twice with phosphate-buffered saline (PBS) and harvested in lysisbuffer (Promega), and assayed for luciferase activity according to the manufacturer's protocol (Promega Dual-Luciferase Reporter Assay System) and for Renilla to correct for transfection efficiency. The relative light units were measured by a Centro LB 960 luminometer (Berthold Technologies, Bad Wildbad, Germany). The results are averages of at least three independent experiments assayed in duplicate  $\pm$ SEM. To compare three or more groups, an ordinary one-way analysis of variance (ANOVA) was performed with a Tukey's multiple comparison test to compare the mean of each group with that of every other group. A statistically significant difference was defined as a *p*-value < 0.05.

### Western blot analysis

Protein expression of the transfected U2OS and HEK293T cells and of adenovirally transduced PPAR $\gamma$ <sup>-/-</sup> MEF-CARs was determined by western blotting. For this, lysates were boiled in Laemmli sample buffer for 5 min at 95 °C. Samples were subjected to SDS-PAGE and transferred to a Millipore membrane (Millipore). Anti-PPAR $\gamma$  (sc-7196; RRID: AB\_654710), anti-Gal4 DBD (sc-510; RRID: AB\_627655), anti-FABP4 (sc-18661; RRID: AB\_2231568), anti-RXR $\alpha$  (sc-553; RRID: AB\_2184874), anti-tubulin (Sigma–Aldrich T9026; RRID: AB\_477593), anti-LPL<sup>42</sup>, anti-FLAG-HRP (Sigma–Aldrich A8592; RRID: AB\_439702), anti-HA (ab9110; RRID: AB\_307019), anti-LgBiT (N710A) were used for detection of the proteins, all at dilution 1:1000 except for the anti-Gal4 DBD antibody which was diluted 1:500. Enhanced chemiluminescence (Amersham Biosciences) was used for visualization. Quantification of band intensity was performed with reference to loading control (tubulin) and PPAR $\gamma$  using the ImageJ Gel Analysis program.

### DNA affinity purifications

Lentiviral vectors for stable expression of PPAR $\gamma$  in U2OS cells were generated by replacing beta-catenin with the PPAR $\gamma$ 2 expression cassette in pLV-CMV-FLAG-betaCatenin-Ires-PURO, a kind gift of Dr. J. de Rooij. Lentiviral particles were produced in HEK293T cells. After lentiviral transduction, stably transduced U2OS cells were selected and maintained on 2  $\mu$ g/ml puromycin. Nuclear extracts from U2OS were prepared as described previously<sup>43</sup>. Oligonucleotides containing either the *CIDE*C wt or *CIDE*C dead motif (Integrated DNA Technologies) with 5' biotinylation of the forward strand (Supplementary Table 1) were annealed using a 1.5 $\times$  molar excess of the reverse strand. For DNA affinity purifications<sup>43</sup>, 500 pmol of DNA oligonucleotides were immobilized using 20  $\mu$ l of Streptavidin-Sepharose bead slurry (GE Healthcare, Chicago, IL). Then, 500  $\mu$ g of nuclear extract and 10  $\mu$ g of non-specific competitor DNA (5  $\mu$ g polyAdT, 5  $\mu$ g polyIdC) were added to each pull-down. After extensive washing, samples were prepared for mass spectrometry analysis or western blotting.

### Mass spectrometry analysis

For mass spectrometry analysis, beads were resuspended in elution buffer (2 M urea, 100 mM TRIS (pH 8.0), 10 mM DTT) and alkylated with 50 mM iodoacetamide. Proteins were digested on beads with 0.25  $\mu$ g of trypsin for 2 h. After the elution of peptides from beads, an additional 0.1  $\mu$ g of trypsin was added, and digestion was continued overnight. Peptides were labeled on Stage tips using dimethyl labeling<sup>43</sup>. Each pull-down was performed in duplicate and label swapping was performed between duplicates to avoid labeling bias. Matching light and heavy peptides were combined and analyzed on an Orbitrap Exploris (Thermo) mass spectrometer with acquisition settings described previously<sup>44</sup>. RAW mass spectrometry data were analyzed with MaxQuant 1.6.0.1 by searching against the UniProt curated human proteome (released June 2017) with standard settings. Protein ratios obtained from MaxQuant were used for outlier calling. An outlier cutoff of 1.5 interquartile ranges in two out of two replicates was used. Western blot analysis of eluted proteins was performed using the FLAG epitope tag for detection.

### Modeling of PPAR $\gamma$ -RXR $\alpha$ 3D structures

To analyze the impact of the E379K mutation in PPAR $\gamma$ , which is located in a functionally less well-characterized region than the R212Q mutation in the hinge region, we used the HADDOCK2.2 web server<sup>45</sup>. As the starting point for the modeling we used the crystal structure of the intact PPAR $\gamma$ :RXR $\alpha$  nuclear receptor complex with DNA (PDB ID 3DZY) (isoform 1)<sup>11</sup>. Both WT and E379K (E351K isoform 1) mutant structures were subjected to a short refinement in explicit solvent using the refinement interface of the HADDOCK server. The mutation was introduced by changing the residue name in the PDB file and letting HADDOCK rebuild any missing atoms.

### Peptide analyses by NMR and CD spectroscopy

Peptides were purchased from TAG Copenhagen A/S (Denmark), purified to  $\geq 95\%$  by reversed-phase HPLC and identities confirmed by mass spectrometry.

For circular dichroism (CD) spectroscopy, samples of 100  $\mu$ M WT-PPAR $\gamma$ <sup>376–385</sup> and E379K-PPAR $\gamma$ <sup>376–385</sup> peptides were prepared in 20 mM Na<sub>2</sub>HPO<sub>4</sub>/NaH<sub>2</sub>PO<sub>4</sub> (pH 7.4). Far-UV CD spectra of the peptides and of a matched buffer sample were recorded from 260 to 190 nm on a Jasco J-810 spectropolarimeter in a 0.1 cm Quartz cuvette (Hellma, Suprasil®) with a Peltier controlled temperature set to 25 °C. Data acquisition was carried out with a scanning speed, 10 nm/min; data pitch, 0.1 nm; accumulations, 10; bandwidth, 1 nm; response time, 2 s. After subtraction of the buffer spectrum, the spectra were smoothed by Fast Fourier Transformation. Helical percentage was calculated using (%H = ( $[\theta]_{222} - 3000$ )/(-36,000 - 3000)) essentially as described<sup>46</sup>.

To assign the resonances of the WT-PPAR $\gamma$ <sup>376–385</sup> and E379K-PPAR $\gamma$ <sup>376–385</sup> peptides, NMR experiments were recorded on 2.3 mM PPAR $\gamma$ <sup>376–385</sup> in 20 mM Na<sub>2</sub>HPO<sub>4</sub>/NaH<sub>2</sub>PO<sub>4</sub> (pH 7.4) at 25 °C on a Bruker Avance NEO 800 MHz spectrometer equipped with a 5 mm CPTXO Cryoprobe C/N-H-D. The following spectra were acquired at natural isotope abundance: 1D <sup>1</sup>H (zgesgp), <sup>1</sup>H-<sup>15</sup>N HSQC (hsqetcfp3gp), <sup>1</sup>H-<sup>13</sup>C HSQC (hsqetgpsisp.2.2), 2D TOCSY (dipsi2esgpph, mixing time 80 ms) and 2D ROESY (roesyegpph, mixing time 250 ms). The spectra were transformed using TopSpin 3.6.2 and analyzed manually in CcpNmr Analysis 2.5.0<sup>47</sup>. All chemical shifts were referenced to internal DSS directly (<sup>1</sup>H) or indirectly (<sup>13</sup>C, <sup>15</sup>N) as described<sup>48</sup>. Secondary chemical shifts of C $\alpha$  were calculated using the random coil set from Kjaergaard et al.<sup>49</sup>.

### NR-Coregulator Interaction analyses

Rosetta pLysS competent bacteria (Novagen, EMD Chemicals Inc., Darmstadt, Germany) were transformed with GST expression plasmids. GST-fusion protein expression was induced with 1 mM IPTG and purified on Glutathione-Sepharose beads (Amersham Biosciences)<sup>39</sup>.

For NR-Coregulator interaction profiling, GST-fusion proteins were eluted from glutathione-sepharose beads (Amersham, Buckinghamshire, UK) using elution buffer (20 mM glutathione, 100 mM Tris pH 8.0, 120 mM NaCl). Proteins were concentrated using Vivaspin centrifugal concentrators (Sartorius, Epsom, UK) and protein concentrations were determined using SDS-PAGE followed by Coomassie Brilliant Blue staining. Assay mixes were prepared on ice in a master 96-Well plate, with 5 nM of purified PPAR- $\gamma$  LBD-GST WT and E379K mutant (see below), TR-FRET Coregulator buffer F (Invitrogen), 25 nM Alexa488-conjugated anti-GST antibody (A11131, Invitrogen), 5 mM DTT, 2% DMSO with or without 1 mM Rosiglitazone. All assays were performed in a PamStation®-96 controlled by EvolveHT software (PamGene International BV, 's-Hertogenbosch, The Netherlands) at 20 °C, at a rate of 2 cycles per minute. Nuclear Receptor PamChip® Arrays (PamGene International BV, 's-Hertogenbosch, The Netherlands) contained 53 peptides<sup>21</sup>. Per array, 25  $\mu$ l of assay mix was transferred from the master plate to the chip using a multichannel pipette. During the period of ligand incubation (-40 minutes), a solution of GST-PPAR $\gamma$ -LBD, fluorescent anti-GST antibody, and ligand was pumped through the porous peptide-containing membrane for 81 cycles at a rate of 2 cycles per minute. Assay mixes were incubated in the arrays for 80 cycles and a tiff format image of every array was obtained at cycles 21, 41, 61, 81 by a CCD camera-based optical system integrated in the PamStation®-96 instrument.

For GST pull-downs, GST or GST-fusion proteins were incubated with 10  $\mu$ l of rabbit reticulolysate containing translated <sup>35</sup>S-labeled protein (TNT T7 Quick Coupled Transcription/Translation Kit, Promega) for 3 hours at 4 °C. After incubation, the beads were washed three times with NETN-buffer and Laemmli sample buffer was added.

Samples were boiled at 95 °C for 5 min and loaded on a 10% SDS-polyacrylamide gel. Proteins were stained with Coomassie Brilliant Blue, and gels were fixed (20% methanol and 10% acetic acid for 10 min) and dried. Radioactive signals were analyzed with a Storm 820 Imager (Molecular Dynamics).

### Protein complementation assays (PCA)

Heterodimerization between PPAR $\gamma$ 2 and hRXR $\alpha$  was analyzed in live cells with the NanoBiT<sup>®</sup> PPI System (Promega)<sup>50</sup>. To generate a protein fusion pair displaying effective complementation of the split luciferase, the Large BiT (LgBiT; 18 kD) of luciferase was fused to the C-terminus of PPAR $\gamma$ 2, while the Small BiT (SmBiT; 1.3 kDa) was fused to the N-terminus of hRXR $\alpha$  (Supplemental Fig. 3a). Mutants were generated using the QuickChange mutagenesis kit (Stratagene). Mutants previously shown to have partially or completely lost heterodimerization capacity (R425C and L464R, respectively<sup>17</sup>) were included as controls.

HEK293T cells were seeded in 96-well plates and transfected with plasmids encoding PPAR $\gamma$ 2-LgBiT (50 ng/well) or mutant versions, and smBiT-hRXR $\alpha$  (50 ng/well) using Xtreme gene (Sigma–Aldrich). After 48 h, cells were washed with PBS and diluted substrate (Nano-Glo<sup>®</sup> Live Cell Assay System; Promega) was added according to the manufacturer's protocol. The relative light units were measured by a Centro LB 960 luminometer (Berthold Technologies, Bad Wildbad, Germany). The results are averages of at least three independent experiments assayed in triplicate  $\pm$ SEM. To compare three or more groups, an ordinary one-way analysis of variance (ANOVA) was performed with a Tukey's multiple comparison test to compare the mean of each group with that of every other group. A statistically significant difference was defined as a *p*-value <0.05. After luminescence analysis, cells were lysed in RIPA buffer, triplicates were pooled and subjected to Western blot analysis, as described above.

### Adenovirus generation and purification

Recombinant adenoviruses containing a hemagglutinin (HA)-tagged mouse PPAR $\gamma$ 2 were generated using AdEasy cloning system (Stratagene)<sup>3</sup>. The Ad-HA-mPPAR $\gamma$ 2-WT<sup>6</sup> was used as a template to generate the mutations R212Q and E379K using QuickChange mutagenesis kit (Stratagene) following the instructions provided by the manufacturer. Successful mutagenesis was verified by Sanger sequencing. The plasmids were linearized and transfected into the HEK293 cell line for amplification and purification using CsCl gradients.

### Adenoviral delivery of PPAR $\gamma$ in PPAR $\gamma$ <sup>-/-</sup> MEF-CAR cells

PPAR $\gamma$ <sup>-/-</sup> MEF-CAR cells<sup>6</sup> were transduced with adenoviral vectors expressing HA-tagged mPPAR $\gamma$ 2-WT, mPPAR $\gamma$ 2-R212Q or mPPAR $\gamma$ 2-E379K. After two hours of virus exposure, the medium was removed, and cells were treated with medium containing either vehicle dimethyl sulfoxide (DMSO) or 1  $\mu$ M rosiglitazone (Alexis) for another 6 hours before harvest for RNA and protein expression analyses and for ChIP- and ATAC-seq.

### Differentiation assay

One-day post confluent PPAR $\gamma$ <sup>-/-</sup> MEF-CAR cells were transduced with adenoviral vectors expressing haemagglutinin (HA)-tagged mPPAR $\gamma$ 2-WT or mutant PPAR $\gamma$ 2. Following 2 h of virus exposure, the medium was removed and replaced by differentiation medium A (DMEM supplemented with 10% FBS (Gibco), 5  $\mu$ g/mL insulin, 1  $\mu$ M dexamethasone, 0.5 mM isobutylmethylxanthine, and 1  $\mu$ M rosiglitazone (Alexis)). After three days, the cells were maintained in differentiation medium B (DMEM supplemented with 10% FBS (Gibco) and 5  $\mu$ g/mL insulin). At day 7, differentiation was evaluated using the Oil-Red-O staining method<sup>17</sup>.

### RNA analysis

RNA extraction, cDNA synthesis, and qPCR were performed as described previously<sup>25</sup>. For RNA-seq analysis, RNA from two independent experiments was prepared in triplicate. After qPCR validation, the triplicates were pooled and prepared for sequencing according to the manufacturer's instructions (Illumina).

Samples were sequenced on Illumina Novaseq 6000 using NovaSeq Control Software v1.3.0, and the quality of sequenced reads was assessed using FastQC (<https://qubeshub.org/resources/fastqc>). Reads were aligned to the mouse genome (mm10) using STAR<sup>51</sup> with default settings. HOMER makeTagDirectory<sup>52</sup> was used to generate tag directories for all conditions on primarily aligned reads. HOMER analyzeRepeats.pl was used to count reads within exons of the mm10 genome with the settings -count exons, -condenseGenes, -noCondensing, -noadj. DESeq2<sup>53</sup> was used to identify differentially regulated genes between conditions.

### ChIP-seq

ChIP was performed as previously described<sup>6</sup>. Samples were sonicated using the Covaris ME220 sonicator (Covaris, Woburn, MA, USA); peak power 75, duty factor 26.66%, 500 cycles/burst for 7.5 minutes. Antibodies directed against hemagglutinin (HA, Abcam Ab9110; RRID: AB\_307019), H3K27ac (Abcam, Ab4729, RRID: AB\_2118291), and MED1 (Bethyl Laboratories, A300–793A; RRID: AB\_577241) were used for immunoprecipitation. For ChIP-seq, the ChIP reactions were scaled to obtain 10 ng DNA. After decrosslinking, the DNA that had undergone ChIP was prepared for sequencing according to the manufacturer's protocol (Illumina). ChIP-seq was performed on two independent experiments.

**Alignment and construction of tag directories.** ChIP-seq libraries were sequenced on the Illumina NovaSeq 6000 using NovaSeq Control Software v1.4.0 and v1.6.0, and the quality of sequenced reads was assessed using FastQC (<https://qubeshub.org/resources/fastqc>). Reads were aligned to the mouse genome (mm10) using STAR<sup>51</sup> with settings: outFilterMismatchNmax 2, alignIntronMax 1, outSJfilterIntronMaxVsReadN 0, and outFilterMatchNmin 25. Picard Tools (Broad Institute <http://broadinstitute.github.io/picard/>) were used to deduplicate primary aligned reads. HOMER makeTagDirectory was used to generate tag directories for all conditions, allowing only one read per position per length of the read (-tbp 1). Due to the uneven sequencing depth of H3K27Ac ChIP-seq samples, one tag directory was down-sampled to 20 mill. reads.

**Identification of PPAR $\gamma$  WT binding sites.** Putative PPAR $\gamma$  binding sites were defined as follows using the HA-PPAR $\gamma$  ChIP-seq data. First, replicates from HA-PPAR $\gamma$ WT treated cells were pooled. Homer findPeaks<sup>52</sup> was used to call putative PPAR $\gamma$  sites using settings -style factor, -localSize 20000, and the pooled tag directory from control samples as reference. Peaks were extended to 500 bp centered around the peak center. Finally, artifact regions were discarded based on the ENCODE Consortium blacklist for the mm10 genome<sup>54</sup>. Peaks with a tag count of fewer than 35 tags were filtered away.

**Identification of sites differentially bound by PPAR $\gamma$ , Med1, or acetylated at H3K27.** PPAR $\gamma$ , Med1 and H3K27Ac ChIP-seq tag counts were quantified in the above defined PPAR $\gamma$ WT binding regions using HOMER annotatePeaks<sup>52</sup> with no normalization of sequencing depth (-noadj). Prior to counting H3K27Ac ChIP-seq tags the PPAR $\gamma$  binding sites were extended  $\pm$ 1.5 kb of the peak center to capture more histone ChIP-seq signal, as histone modifications are generally distributed broadly around transcription factor binding sites. Next, we used DESeq2<sup>53</sup> to (1) call sites that gain Med1 and/or H3K27ac signal upon PPAR $\gamma$ WT expression (denoted PPAR $\gamma$ -target enhancers); (2) call sites that were differentially bound by PPAR $\gamma$ , Med1, or acetylated when



comparing WT and mutant PPAR $\gamma$ ; and (3) obtain PPAR $\gamma$ , Med1, and H3K27Ac counts normalized to the total tag directory size.

**Motif analysis.** HA-PPAR $\gamma$ WT binding sites were scanned for the PPRE motif from the JASPAR database<sup>55</sup> in a region of 200 bp around the peak center and the motif score was extracted using HOMER annotatePeaks<sup>52</sup>. If more than one PPRE motif was identified within a PPAR $\gamma$ -binding region, the motif with the highest motif score was used for further analyses.

De novo motif search was made using Homer findMotifsGenome<sup>52</sup> with motif length of 15–17 bases and searched within  $\pm 100$  bp of peak center of PPAR $\gamma$ -target enhancers. The de novo motif was hereafter used to scan all PPAR $\gamma$ -binding sites using HOMER annotatePeaks.

To analyze the motif score within sections of the motif, position files of PPAR $\gamma$ -binding sites were used to extract the sequence from the FASTA sequence of the mm10 reference genome. The de novo motif was extracted within these sequences using Homer2 find<sup>56</sup>, where the threshold for calling a motif was set to  $-2$ . The motif score was hereafter calculated within sections; 5' extension (base 1–4), PPAR $\gamma$ -half site (base 5–10), and RXR-half site (base 12–17).

### ATAC-seq

ATAC-seq was made in two biological replicates. 100,000 cells were centrifuged  $500 \times g$  for 5 min, 4 °C. The cells were washed once in 200  $\mu$ l DPBS and resuspended in 50  $\mu$ l tagmentation mix (33 mM Tris-acetate, pH 7.8, 66 mM potassium acetate, 10 mM magnesium acetate, 16% dimethylformamide, 0.01% digitonin and 2.5  $\mu$ l Tn5 (Nextera, Illumina)<sup>57</sup>). Tagmentation was performed for 30 min at 37 °C, shaking at 800 rpm. Tagmented DNA was purified using Qiagen PCR purification kit according to the protocol of the manufacturer. Purified tagmented DNA was prepared for sequencing using dual-unique index primers (Illumina TG Nextera<sup>®</sup> XT Index Kit) and Q5 High fidelity DNA polymerase (NEB) under the following PCR conditions: 72 °C 5 min; 98 °C 1 min; 10 cycles 98 °C 10 s, 63 °C 30 s, 72 °C 20 s; 10 °C hold, purified in accordance with the protocol of the manufacturer (Illumina) and sequenced on NovaSeq 6000 using NovaSeq Control Software v.1.6.0.

Quality of sequenced reads was assessed using FastQC (<https://qubeshub.org/resources/fastqc>). Paired-end 50 bp reads were aligned to the mouse genome (mm10) using STAR<sup>51</sup> with settings: outFilterMismatchNmax 2, alignIntronMax 1, outSJfilterIntronMaxVsReadN 0, and outFilterMatchNmin 25. Primarily aligned reads were deduplicated using Picard Tools (Broad Institute <http://broadinstitute.github.io/picard/>) whereafter fragments of length  $\leq 120$  bp were selected for further analyses (nucleosome-free regions) using SAMtools<sup>58</sup>. Tag directories were generated using HOMER makeTagdirectories<sup>52</sup> Using HOMER analyseRepeats<sup>52</sup> ATAC-seq signal was counted within PPAR $\gamma$ -WT peaks extended  $\pm 250$  bp around peak center and in bins of 50 bp in a window of 3000 bp centered at the peak center.

### Enrichment analysis

The number of enhancers in the vicinity of PPAR $\gamma$ -target genes relative to the number of enhancers in the vicinity of non-PPAR $\gamma$ -target genes was determined using BedTools<sup>59</sup>. Two hundred genes not regulated by PPAR $\gamma$  were randomly selected 10 times, and the average number of enhancers was used for normalization.

### Reporting summary

Further information on research design is available in the Nature Portfolio Reporting Summary linked to this article.

### Data availability

The sequence datasets generated in this study have been deposited at NCBI GEO under accession code [GSE199426](https://www.ncbi.nlm.nih.gov/geo/query/acc.cgi?acc=GSE199426). The mass spectrometry

proteomics data have been deposited to the ProteomeXchange Consortium via the PRIDE partner repository with the dataset identifier [PXD036589](https://doi.org/10.1038/s41467-022-34766-9). Processed data used in the preparation of this manuscript are detailed in the Source Data files provided with the manuscript. There are no restrictions on data access. Source data are provided with this paper.

### Code availability

Codes and scripts used to process and analyze data have been deposited to GitHub: <https://github.com/mstahlmadsen/PPARGgamma-lipodystrophy-mutants-reveal-intermolecular-interactions-required-for-enhancer-activation>.

### References

- Lefterova, M. I., Haakonsson, A. K., Lazar, M. A. & Mandrup, S. PPAR $\gamma$  and the global map of adipogenesis and beyond. *Trends Endocrinol. Metab.* **25**, 293–302 (2014).
- Broekema, M. F., Savage, D. B., Monajemi, H. & Kalkhoven, E. Gene-gene and gene-environment interactions in lipodystrophy: lessons learned from natural PPAR $\gamma$  mutants. *Biochim. Biophys. Acta Mol. Cell Biol. Lipids* **1864**, 715–732 (2019).
- Nielsen, R. et al. Genome-wide profiling of PPAR $\gamma$ :RXR and RNA polymerase II occupancy reveals temporal activation of distinct metabolic pathways and changes in RXR dimer composition during adipogenesis. *Genes Dev.* **22**, 2953–2967 (2008).
- Soccio, R. E. et al. Genetic variation determines PPAR $\gamma$  function and anti-diabetic drug response in vivo. *Cell* **162**, 33–44 (2015).
- Ijpenberg, A., Jeannin, E., Wahli, W. & Desvergne, B. Polarity and specific sequence requirements of peroxisome proliferator-activated receptor (PPAR)/retinoid X receptor heterodimer binding to DNA. A functional analysis of the malic enzyme gene PPAR response element. *J. Biol. Chem.* **272**, 20108–20117 (1997).
- Madsen, M. S., Siersbæk, R., Boergesen, M., Nielsen, R. & Mandrup, S. Peroxisome proliferator-activated receptor  $\gamma$  and C/EBP $\alpha$  synergistically activate key metabolic adipocyte genes by assisted loading. *Mol. Cell Biol.* **34**, 939–954 (2014).
- Hernandez-Quiles, M., Broekema, M. F. & Kalkhoven, E. PPAR $\gamma$  in metabolism, immunity, and cancer: unified and diverse mechanisms of action. *Front. Endocrinol. (Lausanne)* **12**, 624112 (2021).
- Helsen, C. & Claessens, F. Looking at nuclear receptors from a new angle. *Mol. Cell Endocrinol.* **382**, 97–106 (2014).
- Chandra, V. et al. The quaternary architecture of RAR $\beta$ -RXR $\alpha$  heterodimer facilitates domain-domain signal transmission. *Nat. Commun.* **8**, 868 (2017).
- Shao, D. et al. Interdomain communication regulating ligand binding by PPAR $\gamma$ . *Nature* **396**, 377–380 (1998).
- Chandra, V. et al. Structure of the intact PPAR $\gamma$ -RXR $\alpha$  nuclear receptor complex on DNA. *Nature* **456**, 350–356 (2008).
- Osz, J. et al. Solution structures of PPAR $\gamma$ 2/RXR $\alpha$  complexes. *PPAR Res.* **2012**, 701412 (2012).
- Rochel, N. et al. Common architecture of nuclear receptor heterodimers on DNA direct repeat elements with different spacings. *Nat. Struct. Mol. Biol.* **18**, 564–570 (2011).
- Bernardes, A. et al. Low-resolution molecular models reveal the oligomeric state of the PPAR and the conformational organization of its domains in solution. *PLoS ONE* **7**, e31852 (2012).
- Majithia, A. R. et al. Prospective functional classification of all possible missense variants in PPARG. *Nat. Genet.* **48**, 1570–1575 (2016).
- Sorkina, E. L. et al. Development of metabolic syndrome at a young age as a manifestation of familial partial lipodystrophy type 3 (PPARG mutation): the first description of its clinical case in Russia. *Diabetes Mellit.* **18**, 99–105 (2015).
- Jeninga, E. H. et al. Impaired peroxisome proliferator-activated receptor  $\gamma$  function through mutation of a conserved salt

- bridge (R425C) in familial partial lipodystrophy. *Mol. Endocrinol.* **21**, 1049–1065 (2007).
18. Schoonjans, K. et al. PPARalpha and PPARgamma activators direct a distinct tissue-specific transcriptional response via a PPRE in the lipoprotein lipase gene. *EMBO J.* **15**, 5336–5348 (1996).
  19. Matsusue, K. et al. Hepatic steatosis in leptin-deficient mice is promoted by the PPARγ target gene Fsp27. *Cell Metab.* **7**, 302–311 (2008).
  20. Broekema, M. F. et al. Natural helix 9 mutants of PPARgamma differently affect its transcriptional activity. *Mol. Metab.* **20**, 115–127 (2019).
  21. Koppen, A. et al. Nuclear receptor-coregulator interaction profiling identifies TRIP3 as a novel peroxisome proliferator-activated receptor gamma cofactor. *Mol. Cell Proteom.* **8**, 2212–2226 (2009).
  22. Haakonsson, A., Stahl Madsen, M., Nielsen, R., Sandelin, A. & Mandrup, S. Acute genome-wide effects of rosiglitazone on PPARγ transcriptional networks in adipocytes. *Mol. Endocrinol.* **27**, 1536–1549 (2013).
  23. Step, S. E. et al. Anti-diabetic rosiglitazone remodels the adipocyte transcriptome by redistributing transcription to PPARγ-driven enhancers. *Genes Dev.* **28**, 1018–1028 (2014).
  24. Loft, A. et al. Browning of human adipocytes requires KLF11 and reprogramming of PPARgamma superenhancers. *Genes Dev.* **29**, 7–22 (2015).
  25. Bugge, A. et al. A novel intronic peroxisome proliferator-activated receptor gamma enhancer in the uncoupling protein (UCP) 3 gene as a regulator of both UCP2 and -3 expression in adipocytes. *J. Biol. Chem.* **285**, 17310–17317 (2010).
  26. Tontonoz, P. et al. Adipocyte-specific transcription factor ARF6 is a heterodimeric complex of two nuclear hormone receptors, PPAR gamma and RXR alpha. *Nucleic Acids Res.* **22**, 5628–5634 (1994).
  27. Wu, Z. et al. Cross-regulation of C/EBP alpha and PPAR gamma controls the transcriptional pathway of adipogenesis and insulin sensitivity. *Mol. Cell* **3**, 151–158 (1999).
  28. El-Jack, A. K., Hamm, J. K., Pilch, P. F. & Farmer, S. R. Reconstitution of insulin-sensitive glucose transport in fibroblasts requires expression of both PPARgamma and C/EBPalpha. *J. Biol. Chem.* **274**, 7946–7951 (1999).
  29. Tontonoz, P., Hu, E., Graves, R. A., Budavari, A. I. & Spiegelman, B. M. mPPAR gamma 2: tissue-specific regulator of an adipocyte enhancer. *Genes Dev.* **8**, 1224–1234 (1994).
  30. Voss, T. C. & Hager, G. L. Dynamic regulation of transcriptional states by chromatin and transcription factors. *Nat. Rev. Genet.* **15**, 69–81 (2014).
  31. Meijnsing, S. H. et al. DNA binding site sequence directs glucocorticoid receptor structure and activity. *Science* **324**, 407–410 (2009).
  32. Achermann, J. C., Schwabe, J., Fairall, L. & Chatterjee, K. Genetic disorders of nuclear receptors. *J. Clin. Invest* **127**, 1181–1192 (2017).
  33. Hsu, M.-H., Palmer, C. N. A., Song, W., Griffin, K. J. & Johnson, E. F. A carboxyl-terminal extension of the zinc finger domain contributes to the specificity and polarity of peroxisome proliferator-activated receptor DNA binding\*. *J. Biol. Chem.* **273**, 27988–27997 (1998).
  34. Juge-Aubry, C. et al. DNA binding properties of peroxisome proliferator-activated receptor subtypes on various natural peroxisome proliferator response elements. Importance of the 5'-flanking region. *J. Biol. Chem.* **272**, 25252–25259 (1997).
  35. Dron, J. S. et al. Six years' experience with LipidSeq: clinical and research learnings from a hybrid, targeted sequencing panel for dyslipidemias. *BMC Med. Genomics* **13**, 23 (2020).
  36. Sherry, S. T. et al. dbSNP: the NCBI database of genetic variation. *Nucleic Acids Res.* **29**, 308–311 (2001).
  37. Lek, M. et al. Analysis of protein-coding genetic variation in 60,706 humans. *Nature* **536**, 285–291 (2016).
  38. Ramos Pittol, J. M. et al. FXR isoforms control different metabolic functions in liver cells via binding to specific DNA motifs. *Gastroenterology* **159**, 1853–1865.e10 (2020).
  39. Kalkhoven, E., Teunissen, H., Houweling, A., Verrijzer, C. P. & Zan-tema, A. The PHD type zinc finger is an integral part of the CBP acetyltransferase domain. *Mol. Cell Biol.* **22**, 1961–1970 (2002).
  40. Vila-Brau, A., De Sousa-Coelho, A. L., Goncalves, J. F., Haro, D. & Marrero, P. F. Fsp27/CIDEA is a CREB target gene induced during early fasting in liver and regulated by FA oxidation rate. *J. Lipid Res.* **54**, 592–601 (2013).
  41. Gurnell, M. et al. A dominant-negative peroxisome proliferator-activated receptor gamma (PPARgamma) mutant is a constitutive repressor and inhibits PPARgamma-mediated adipogenesis. *J. Biol. Chem.* **275**, 5754–5759 (2000).
  42. Page, S., Judson, A., Melford, K. & Bensadoun, A. Interaction of lipoprotein lipase and receptor-associated protein. *J. Biol. Chem.* **281**, 13931–13938 (2006).
  43. Makowski, M. M. et al. An interaction proteomics survey of transcription factor binding at recurrent TERT promoter mutations. *Proteomics* **16**, 417–426 (2016).
  44. Santos-Barrapedro, I., van Mierlo, G. & Vermeulen, M. Off-the-shelf proximity biotinylation for interaction proteomics. *Nat. Commun.* **12**, 5015 (2021).
  45. van Zundert, G. C. P. et al. The HADDOCK2.2 web server: user-friendly integrative modeling of biomolecular complexes. *J. Mol. Biol.* **428**, 720–725 (2016).
  46. Padmanabhan, S., Marqusee, S., Ridgeway, T., Laue, T. M. & Baldwin, R. L. Relative helix-forming tendencies of nonpolar amino acids. *Nature* **344**, 268–270 (1990).
  47. Vranken, W. F. et al. The CCPN data model for NMR spectroscopy: development of a software pipeline. *Proteins* **59**, 687–696 (2005).
  48. Wishart, D. S. et al. 1H, 13C and 15N chemical shift referencing in biomolecular NMR. *J. Biomol. NMR* **6**, 135–140 (1995).
  49. Kjaergaard, M., Brander, S. & Poulsen, F. M. Random coil chemical shift for intrinsically disordered proteins: effects of temperature and pH. *J. Biomol. NMR* **49**, 139–149 (2011).
  50. Dixon, A. S. et al. NanoLuc complementation reporter optimized for accurate measurement of protein interactions in cells. *ACS Chem. Biol.* **11**, 400–408 (2016).
  51. Dobin, A. et al. STAR: ultrafast universal RNA-seq aligner. *Bioinformatics* **29**, 15–21 (2013).
  52. Heinz, S. et al. Simple combinations of lineage-determining transcription factors prime cis-regulatory elements required for macrophage and B cell identities. *Mol. Cell* **38**, 576–589 (2010).
  53. Love, M. I., Huber, W. & Anders, S. Moderated estimation of fold change and dispersion for RNA-seq data with DESeq2. *Genome Biol.* **15**, 550 (2014).
  54. Amemiya, H. M., Kundaje, A. & Boyle, A. P. The ENCODE blacklist: identification of problematic regions of the genome. *Sci. Rep.* **9**, 9354 (2019).
  55. Fornes, O. et al. JASPAR 2020: update of the open-access database of transcription factor binding profiles. *Nucleic Acids Res.* **48**, D87–d92 (2020).
  56. Huppert, T. J., Diamond, S. G., Franceschini, M. A. & Boas, D. A. HomER: a review of time-series analysis methods for near-infrared spectroscopy of the brain. *Appl. Opt.* **48**, D280–D298 (2009).
  57. Chen, X., Miragaia, R. J., Natarajan, K. N. & Teichmann, S. A. A rapid and robust method for single cell chromatin accessibility profiling. *Nat. Commun.* **9**, 5345 (2018).
  58. Li, H. et al. The Sequence Alignment/Map format and SAMtools. *Bioinformatics* **25**, 2078–2079 (2009).
  59. Quinlan, A. R. & Hall, I. M. BEDTools: a flexible suite of utilities for comparing genomic features. *Bioinformatics* **26**, 841–842 (2010).
  60. Morin, A. et al. Collaboration gets the most out of software. *Elife* **2**, e01456 (2013).

## Acknowledgements

This work was supported by grants from the Independent Research Fund Denmark (Sapere Aude Advanced grant no. 12-125524 to S.M.), the Danish National Research Foundation (DNRF grant no. 141 to the Center for Functional Genomics and Tissue Plasticity (ATLAS) (to S.M.)), the Novo Nordisk Foundation (support to S.M. through the NNF Center for Stem Cell Biology (NNF17CC0027852) and to BBK through the NNF Challenge center REPIN (NNF18OC0033926) and cOpenNMR (NNF18OC0032996), (the Villum Foundation (support to S.M. through the Villum Center for Bioanalytical Sciences and to K.N.N through grant VYI25397). The Vermeulen lab is part of the Oncode Institute, which is partly funded by the Dutch Cancer Society. We thank members of the Kalkhoven, Mandrup and Van Mil laboratories for helpful discussions and Dr. Wilko Spiering for clinical assessment. We thank Dr. Natasja Rochel and Dr. Bruno Klaholz for kindly providing the SAXS data of the DNA-bound PPAR $\gamma$ /RXR $\alpha$  heterodimer structure, Marijke Baltissen and Dr. Cornelia G. Spruijt for expert technical advice, Dr. Johan de Rooij for the pLV-CMV-FLAG-betaCatenin-Ires-PURO vector, and Dr. A. Bensa-doun for kindly providing the antibody against mouse LPL.

## Author contributions

M.S.M., M.F.B., M.R.M., A.K., A.B., C.G., E.G.K.T., D.W., M.E.G.K., M.G.K., N.H., and J.M.R.P. designed and performed experiments and analyzed the data, M.S.M. and M.R.M. performed computational analyses, A.M.J.J.B. and B.K. performed detailed protein structure analyses, H.M. and D.C. performed patient identification and detailed clinical assessment, E.K., S.M., S.K., F.C.P.H., H.M., S.W.C.M., M.V., B.K., D.C., and K.N.N. supervised the study, M.S.M., M.F.B., S.M., and E.K. wrote the manuscript. S.M. and E.K. were responsible for the overall project management and co-supervised the research.

## Competing interests

The authors declare no competing interests.

## Additional information

**Supplementary information** The online version contains supplementary material available at <https://doi.org/10.1038/s41467-022-34766-9>.

**Correspondence** and requests for materials should be addressed to Susanne Mandrup or Eric Kalkhoven.

**Peer review information** *Nature Communications* thanks the anonymous reviewer(s) for their contribution to the peer review of this work. Peer reviewer reports are available.

**Reprints and permissions information** is available at <http://www.nature.com/reprints>

**Publisher's note** Springer Nature remains neutral with regard to jurisdictional claims in published maps and institutional affiliations.

**Open Access** This article is licensed under a Creative Commons Attribution 4.0 International License, which permits use, sharing, adaptation, distribution and reproduction in any medium or format, as long as you give appropriate credit to the original author(s) and the source, provide a link to the Creative Commons license, and indicate if changes were made. The images or other third party material in this article are included in the article's Creative Commons license, unless indicated otherwise in a credit line to the material. If material is not included in the article's Creative Commons license and your intended use is not permitted by statutory regulation or exceeds the permitted use, you will need to obtain permission directly from the copyright holder. To view a copy of this license, visit <http://creativecommons.org/licenses/by/4.0/>.

© The Author(s) 2022

<sup>1</sup>Functional Genomics and Metabolism Research Unit, Department of Biochemistry and Molecular Biology, University of Southern Denmark, Odense, Denmark. <sup>2</sup>Center for Molecular Medicine, University Medical Center Utrecht, Utrecht University, Utrecht, The Netherlands. <sup>3</sup>Department of Molecular Biology, Faculty of Science, Radboud Institute for Molecular Life Sciences, Oncode Institute, Radboud University Nijmegen, 6525 Nijmegen, GA, The Netherlands. <sup>4</sup>Department of Biology, University of Copenhagen, Copenhagen, Denmark. <sup>5</sup>Faculty of Science—Chemistry, Bijvoet Centre for Biomolecular Research, Utrecht University, Utrecht, The Netherlands. <sup>6</sup>Division of Human Nutrition, Nutrition, Metabolism and Genomics Group, Wageningen University, Wageningen, The Netherlands. <sup>7</sup>Internal Medicine, Rijnstate Hospital, Arnhem, The Netherlands. <sup>8</sup>Department of Vascular Medicine, University Medical Center Utrecht, Utrecht University, Utrecht, The Netherlands. <sup>9</sup>Center for Metabolic Diseases, Leuven University Hospitals, Leuven, Belgium. <sup>10</sup>Present address: Department of Human Genetics, Amsterdam UMC, Vrije Universiteit Amsterdam, Amsterdam, The Netherlands. <sup>11</sup>Present address: Gubra, Hørsholm, Denmark. <sup>12</sup>Present address: Princess Máxima Center for Pediatric Oncology, Utrecht, the Netherlands. <sup>13</sup>Present address: Institute of Biochemistry and Center for Molecular Biosciences Innsbruck, University of Innsbruck, Innsbruck, Austria. <sup>14</sup>These authors contributed equally: Maria Stahl Madsen, Marjolaine F. Broekema. <sup>15</sup>These authors jointly supervised this work: Susanne Mandrup, Eric Kalkhoven. ✉ e-mail: [s.mandrup@bmb.sdu.dk](mailto:s.mandrup@bmb.sdu.dk); [e.kalkhoven@umcutrecht.nl](mailto:e.kalkhoven@umcutrecht.nl)